Title

An Anatomical and Physiological Basis for Coincidence Detection Across Time Scales in the Auditory System

Authors

Lauren J Kreeger[1], Suraj Honnuraiah[1,2], Sydney Maeker[1], Siobhan Shea[1], Gord Fishell[1,2], and Lisa V Goodrich[1,*]

[1]Harvard Medical School, Department of Neurobiology, Boston, MA 02115, USA
[2]Stanley Center for Psychiatric Research, Broad Institute of MIT and Harvard, Cambridge, MA 02142, USA
*Correspondence: lisa_goodrich@hms.harvard.edu (L.V.G.)

Summary

Coincidence detection is a common neural computation that identifies co-occurring stimuli by integration of inputs. In the auditory system, octopus cells act as coincidence detectors for complex sounds that include both synchronous and sequenced combinations of frequencies. Octopus cells must detect coincidence on both the millisecond and submillisecond time scale, unlike the average neuron, which integrates inputs over time on the order of tens of milliseconds. Here, we show that octopus cell computations in the cell body are shaped by inhibition in the dendrites, which adjusts the strength and timing of incoming signals to achieve submillisecond acuity. This mechanism is crucial for the fundamental process of integrating the synchronized frequencies of natural auditory signals over time.

Introduction

Perception depends on the ability of neurons to encode discrete features of complex external stimuli. These computations are determined by the nature of information received from the periphery, the nature and position of the synapses, and the biophysical properties of the target neuron. For instance, in the auditory system, spiral ganglion neurons (SGNs) encode sound information from hair cells in the cochlea and distribute it to specialized target neurons in the cochlear nucleus complex (CNC) that extract individual elements of the original sound, such as frequency, phase, amplitude, and timing (Fig. 1). The outcome of each dedicated computation continues to be processed through parallel ascending pathways and ultimately to the cortex, where the auditory features are reassembled to generate a percept. Thus, understanding how these first computations are made is a key step towards deciphering the basis of perception.

To generate accurate percepts of complex auditory stimuli, neurons must compute both what frequencies are present and when those frequencies occur across multiple time scales. For instance, overlapping sound stimuli, such as two competing speakers in a noisy room, are perceptually distinguished by correctly binding together frequencies with coherent onsets that then continue to change together over time[1]. Such computations require coincidence detection that can accurately encode co-occurring frequencies with submillisecond precision. Timing on the order of milliseconds is especially important for speech, where sounds contain multiple frequencies that occur simultaneously and in a specific sequence. Frequency information is communicated by SGNs, whose auditory nerve fibers (ANFs) project through the eighth nerve, bifurcate, and spread tonotopically to fill each division of the CNC. In addition, SGNs fall into physiologically distinct subtypes that are recruited at different intensities, thereby allowing sounds to be detected across a wide dynamic range and in the presence of background noise. Many target neurons receive ANF inputs from a limited range of frequencies and fire at the onset of the sound, effectively breaking it up into its frequency components. This presents a challenge for perception as auditory circuits must ultimately bind together co-occurring frequencies while also retaining information about their sequence to locate and recognize sounds.

In the mammalian auditory system, precise encoding of broadband timing information begins with the octopus cells of the CNC. Octopus cells are excitatory neurons that bind together co-occurring frequency information on a submillisecond timescale and send this information along one of the parallel ascending pathways in the auditory brainstem. Octopus cells are named for their large-diameter tentacle-like dendrites[2,3], which are oriented unidirectionally across a tonotopic array of ANFs such that each neuron integrates inputs from a wide range of frequencies, which is reflected in the unusually broad low threshold portions of their tuning curves[4–7]. ANFs provide the major excitatory inputs onto octopus cells. Biophysically, octopus cells have low input resistances near rest (~4MΩ), fast time constants (~200μs), and a large low-voltage-activated potassium conductance (~40nS at rest) that give these cells impressively narrow windows of coincidence detection on the order of 1 millisecond[8–15]. This combination of receiving ANF innervation across broad frequencies and their biophysical specializations establish octopus cells as spectrotemporal coincidence detectors that can reliably encode the timing of complex stimuli, such as the broadband transients found in speech and other natural sounds[12,16,17]. Fittingly, *in vivo* recordings from octopus cells demonstrate their ability to phase lock to broadband transients at rates up to 1kHz[18–20]. Moreover, computational models of octopus cells demonstrate that onset responses are governed by the cell's biophysical specializations and are, in large part, the result of temporal summation of excitation[21–27]. The simplicity of its connectivity combined with the precision of its temporal computations makes the octopus cell an attractive model for understanding how specialized anatomical and electrophysiological properties contribute to neuronal computations.

Although the octopus cell's integration of ANF inputs within a very narrow time frame enables canonical coincidence detection, such a model does not explain how other temporal features of sound stimuli are encoded. Indeed, octopus cells encode spectrotemporal sequences, like frequency modulated sounds, that likely require further circuit specializations[28]. Although threshold somatic depolarization can be sufficient to activate an octopus cell[22], the vast majority of synapses are found on dendrites. Further, ANF inputs are organized tonotopically along octopus cell dendrites, with inputs from high frequency regions located more distal than those from low frequency regions. Dendritic morphology, passive cable properties, active resting membrane properties, and the spatial and temporal relationship between synaptic inputs can all impact EPSP summation as excitation sweeps across the dendritic arbor and towards the soma. This raises the possibility that computations made in the dendrites influence the effective window of coincidence detection by the octopus cell.

Here, we sought to define the circuit mechanisms that allow octopus cells to act as coincidence detectors across time scales. We generated a comprehensive anatomical and physiological map of excitatory and synaptic inputs onto octopus cell somas and dendrites and examined how this circuit organization influences octopus cell activation. Through a combination of *in vitro* experiments and computational modeling, we show that octopus cell firing is shaped by dendritic inhibition. Thus, octopus cells depend on compartmentalized computations that enable preservation of timing information across multiple time scales, which is fundamental for the spectrotemporal integration of natural auditory stimuli.

Results

Excitatory and inhibitory synapse distribution establishes somatic and dendritic domains.

To determine the wiring pattern that drives octopus cell computations, we generated a detailed map of excitatory and inhibitory synaptic inputs (Fig. 1), with awareness of excitatory input subtype identity (Fig. 2). Overall, octopus cells receive abundant excitatory VGLUT1+ innervation from ANFs[29,30] and sparse inhibitory innervation from glycinergic neurons, as visualized using the glycinergic Cre driver *Glyt2*$^{\mathrm{Cre}}$ and a synaptophysin-tdTomato (syp) fusion protein reporter (Ai34). Although sparse, inhibitory inputs are reliably nestled between neatly tiled ANF inputs, especially on octopus cell dendrites (Fig. 1B,C).

Quantification of the number and distribution of presynaptic puncta onto octopus cells revealed marked differences in the balance of excitation and inhibition in the somatic and dendritic compartments. Since innervation patterns have never been systematically analyzed, we made three-dimensional reconstructions of 16 octopus cells and all of their excitatory ANF (n = 8 cells, 4 mice) and glycinergic (n = 8 cells, 3 mice) inputs. Octopus cells were visualized using a Thy1 reporter and presynaptic puncta were labeled with the syp reporter driven either by *Foxg1*$^{\mathrm{Cre}}$ (which is active in all ANFs) or *Glyt2*$^{\mathrm{Cre}}$. Consistent with qualitative assessment, the density of ANF inputs was much higher (10.7 ± 3.0 ANF puncta/100μm^2) than that of inhibitory inputs (4.2 ± 0.8 puncta/100μm^2, Fig. 1D). Moreover, the relative proportions of excitatory and inhibitory inputs differed in the soma and dendrites (Fig. 1E). On somas, ANFs provided dense innervation that continued into the proximal dendrite, then gradually declined. By contrast, somas received very few inhibitory inputs, which were instead evenly distributed along the dendrite. As a result, each octopus cell had strikingly different ratios of excitatory and inhibitory puncta on the soma (7:1) and on the dendrite (2.5:1), suggesting that each compartment contributes differentially to the final computation made by the octopus cell (Fig. 1F).

The majority of ANF synapses on octopus cells are from type Ia SGNs.

Although uniformly glutamatergic, ANFs exhibit stereotyped physiological differences that could affect the nature of their inputs onto octopus cells and hence influence their ability to act as coincidence detectors[31–34,34,35]. With the recent discovery that there are three molecularly distinct SGN subtypes that correlate with previously shown physiological groups[36–42], we further categorized ANF inputs based on SGN subtype identity. Ia SGNs were distinguished from Ib and Ic SGNs using an intersectional approach (Fig. 2). Consistent with the restricted expression of *Ntng1* in Ib and Ic SGNs[39,40,42], the *Ntng1*$^{\mathrm{Cre}}$ transgenic mouse line[43] drove expression of a tdTomato reporter in a subset of SGNs that expressed either moderate (CR+, Ib) or very low (CR-, Ic) levels of calretinin and were reliably segregated from high calretinin (CR++) Ia SGNs (Fig. 2B, Supp. Fig. 1). *Ntng1*$^{\mathrm{Cre}}$-labeled Ib and Ic SGNs (Ib/c) accounted for 60.1 ± 2.6% of the entire population, with 28.5 ± 12.2% Ib SGNs (tdT+ CR+) and thus 31.6% Ic SGNs and 39.9 ± 2.6% Ia SGNs (Fig. 2C: *n* = 1599 neurons, 4 mice; mean ± SD). Further, the proportion of Ia (tdT- CR++) and Ib/c SGNs matched scRNA-seq estimates, indicating that this approach provides full coverage. SGN subtype identity was further confirmed by examining the spatial organization of SGN peripheral processes as they pass through the habenula and make synapses on IHCs in the cochlea (Supp. Fig. 1A-E).

Although *Ntng1*^{Cre} also drives expression broadly in the brain, labeling was restricted to ANFs in the ventral cochlear nucleus (VCN), where octopus cells reside (Supp. Fig. 1F). In the VCN, the pattern of expression in SGN central axons also matched expectations, with some tdT+ CR+ Ib ANFs and some tdT+ CR- Ic ANFs (Supp. Fig. 2G). Thus, *Ntng1*^{Cre}-driven expression of syp is an appropriate tool for mapping subtype-specific connectivity onto octopus cells.

We found that octopus cells are dominated by inputs from Ia ANF fibers, which are the fibers with the lowest thresholds and highest rates of spontaneous activity. Octopus cell dendrites received 4.1 ± 1.0 puncta/100μm^2 from Ib/c ANFs (Fig. 2D, magenta: *n* = 9 cells, 5 mice; mean ± SD), accounting for 38% of the total ANF density. Given that *Ntng1*-tdT+ cells account for 60.1% of the SGN population (Fig. 2C, magenta), Ib/c inputs were significantly underrepresented on octopus cells. Octopus cells receive similarly low innervation from Ic inputs (Supp. Fig. 2H-I: *n* = 6 cells, 2 mice), as estimated from the degree of sparse labeling achieved by *Myo15*$^{\mathrm{iCre}}$ (Supp. Fig. 2A-F) and the expected proportion of Ic SGNs in the ganglion (Supp. Fig. 2F). By contrast, Ia ANFs accounted for 62% of ANF synapses on octopus cells (6.6 ± 1.0 puncta/100μm^2), although Ia SGNs comprise only ~40% of the total population. All three subtypes showed the same overall distribution from the soma to the distal dendrite. Together, excitatory and inhibitory puncta densities in our innervation maps indicate the average octopus cell receives ~1035 ANF synapses (642 Ia ANF, 393 Ib/c ANF) and ~354 inhibitory synapses. Additionally, the majority of synapses on the average octopus cell (83%) are found on dendrites, highlighting their critical role in the octopus cell computation.

The resulting octopus cell maps showed the same basic wiring patterns regardless of where each cell was positioned in the octopus cell area. The tonotopic position of all reconstructed octopus cell somas was estimated in 3D reconstructions aligned to a normalized CNC model of tonotopy[44]. Octopus cells had similar morphologies (Supp. Fig. 3A-G) and patterns of synaptic innervation (Supp. Fig. 1H-M) regardless of where they were positioned along the tonotopic axis. Thus, we have established definitive wiring diagrams for octopus cells that include the numbers and types of three kinds of ANF input and of glycinergic inhibitory inputs onto both the soma and the dendrites. These inputs ultimately determine whether or not an octopus cell will fire an action potential and thus transmit information along ascending pathways to influence how sound is perceived.

ANF inputs to octopus cells have stable response amplitudes over a range of frequencies.

Whether or not an octopus cell responds to its inputs depends on when and how EPSPs travel to then summate in the soma. Almost nothing is known about how the different SGN subtypes transmit information to their central targets. Therefore, we performed *in vitro* whole-cell current clamp recordings of octopus cells (Fig. 3) while using ChR2 to stimulate either all ANFs (*Foxg1*-ChR2) or only Ib/c ANFs (*Ntng1*-ChR2). Trains of ChR2-evoked ANF stimulation led to paired-pulse depression both in total ANF-induced EPSPs (Fig. 3B, black: n = 8 cells, 5 mice) and Ib/c ANF-induced EPSPs (Fig. 3B, magenta: n = 7 cells, 6 mice). There were no differences in paired-pulse plasticity between these populations at any frequency ($p>0.35$ at all interstimulus intervals, Tukey's HSD), although the variability was higher in the Ib/c population compared to the total ANF population (at 20ms: SD= 0.11, SD=0.24, respectively).

Although we found no striking differences across subtypes, our results did raise the possibility that depression of excitatory inputs could shape octopus cell responses. Indeed, synaptic depression in the auditory brainstem is common and is believed to be a useful mechanism for reliably transmitting temporal information when inputs are noisy[45,46]. However, while ChR2-stimulated ANF EPSPs were depressing, electrically induced ANF EPSPs had higher paired-pulse ratios and were mildly facilitating at short (20ms) intervals (Fig. 3B-C, open circles: n = 5 cells, 3 mice). This is in contradiction with previous results that demonstrated short-term depression of ANF inputs to octopus cells[45,47], although with higher non-physiological levels of extracellular calcium. Indeed, higher calcium concentrations (2.4mM) resulted in short-term depression at 50Hz of electrical stimulation (Fig. 3C, grey: n = 3 cells, 2 mice), though not to the degree observed when using full-field, ChR2-evoked inputs. Therefore, electrically-evoked EPSPs measured under physiological levels of extracellular calcium (1.4mM) are more stable than previously reported, consistent with an octopus cell's ability to reliably respond to click trains *in vivo*[4,6,19,48].

***Inhibition is electrically isolated to dendrites*.**

Given the higher density of glycinergic synapses on octopus cell dendrites, we considered the possibility that somatic and dendritic compartments contribute differently to the final computation octopus cells make. A role for inhibition has never been incorporated into octopus cell models as previous efforts failed to reveal physiological evidence of functional inhibitory synapses onto octopus cells either *in vitro*[11,49,50] or *in vivo*[28]*.* Since inhibitory synapses are primarily located on octopus cell dendrites, we posited that their voltage spread to the soma is limited given the extremely low input resistance of octopus cell somas. Consequently, light-evoked (*Glyt2*-ChR2*)* inhibitory post synaptic potentials (IPSPs) were not detected in octopus cell somas during whole-cell current clamp recordings from P30-45 mice. To decrease electrotonic isolation of the dendrites and increase input resistance, we pharmacologically blocked voltage-gated potassium (K_v) and hyperpolarization-activated cyclic nucleotide-gated channels (HCN) using 100μM 4-Aminopyridine (4-AP) and 50μM ZD 7288. This cocktail increased octopus cell membrane resistance (Fig. 4A). To isolate inhibition, 15μM 2,3-dioxo-6-nitro-7-sulfamoyl-benzo[f]quinoxaline (NBQX) was added to block spontaneous EPSPs. By increasing input resistance, we were able to detect light-evoked glycinergic IPSPs in recordings from octopus cell somas (Fig. 4B).

To determine the types of glycinergic receptors contributing to IPSPs, we pharmacologically blocked subsets of glycine receptors. IPSPs were reduced upon addition of 20µM picrotoxin (PTX), which blocks homomeric glycine receptors[51–53]. Addition of 100µM cyclothiazide (CTZ), which blocks α2-containing homomeric and heteromeric glycine receptors[54,55], nearly abolished the remaining IPSPs, and responses were fully abolished with application of 500nM strychnine (STN), which blocks all glycinergic transmission (Fig. 4C). Collectively, these data demonstrate that glycinergic synaptic contacts onto octopus cell dendrites are functional. Additionally, glycine receptor subunit composition implicates a role for both large conductance extrasynaptic β-subunit lacking homomeric receptors and synaptically localized α2β receptors with slower kinetics[56–58].

To further define the impact of IPSPs on octopus cell activity, we developed an improved biophysically and anatomically accurate model of octopus cells based on our findings (Supp. Fig. 4)[17,59]. This model performed as predicted based on our experimental results. As in our current-clamp recordings, stimulation of dendritic glycinergic conductances resulted in negligible hyperpolarizing voltage changes (Fig. 4E) in control conditions. Removal of K_v and HCN conductances in the model changed the input resistance and current-voltage relationship of the neuron, resulting in reduced electronic isolation (Fig. 4D, blue). With increased input resistance, IPSPs measured at the soma were similar to *in vitro* recordings (Fig. 4E,F). Thus, our model confirms that dendritic IPSPs can elicit somatic hyperpolarizations octopus cell responses when electrotonic dendritic isolation is reduced.

While blocking K_v and HCN allowed us to reveal IPSPs at the soma, 4-AP increases the duration of the already unphysiological ChR2-evoked presynaptic action potential[60], resulting in altered release probabilities and synaptic properties, amongst other caveats[61]. Additionally, because the resting potential of octopus cells is regulated by both K_v and HCN channels[10], blocking this critical conductance will impact the driving force of chloride and result in an increased IPSP measured at the soma. To directly test if the increase in somatically-measured IPSP amplitude is the result of changes in input resistance or the result of pharmacological confounds, we used our octopus cell model to measure somatic voltages and dendritic currents while K_v and HCN channels were blocked (Fig. 4G). While soma-measured IPSPs increased in size with K_v and HCN block (Fig. 4G, blue), dendrite-measured currents did not change (Fig 4G, dark orange, light orange), indicating there are inhibitory currents on octopus dendrites that are small or undetectable at the soma due to the cell's input resistance.

Inhibition decreases magnitude and advances timing of dendritic ANF inputs to octopus cells.

Our octopus cell model also demonstrated that dendritic inhibition has the potential to impact coincidence detection computations in the soma. ANF synapses onto octopus cell dendrites are arranged tonotopically, with higher frequency ANFs from the base of the cochlea terminating on the distal dendrites and lower frequency ANFs from more apical positions terminating more proximally. This organization has long been hypothesized to re-synchronize coincidentally firing ANFs that are activated at slightly different times due to the time it takes for the sound stimulus to travel from the base to the apex of the cochlea[17]. To test how inhibition in the dendrites might further shape coincidence detection, we used our model to explore the influence of synapses at varying locations along the dendritic tree. By placing inhibitory synapses on proximal or distal dendrites and moving the location of excitation relative to inhibition, we modelled the effect of on-path and off-path inhibition[62] on somatically recorded EPSPs (Fig. 5A, Supp. Fig. 5). For both on-path (Fig. 5B, D) and off-path (Fig. 5C, E) inhibition, the model predicts that inhibition reduces the amplitude of and advances the timing of EPSPs as measured at the soma, which would in turn improve the ability of the octopus cell to encode coincident changes in frequency during continuous auditory stimuli.

We directly tested if temporally coincident excitation and inhibition affects the integration of ANF inputs as they travel towards the soma by coincidently activating ANFs and glycinergic inputs *in vitro* (Fig. 5F). In these experiments, the octopus cell properties were not altered pharmacologically and inhibition was undetectable or only visible with averaging over many sweeps (Fig. 5G, blue). When synaptic inhibition was evoked with excitation, the soma-recorded EPSPs were smaller than when excitation was evoked alone (Fig. 5G: *n* = 8 cells, 6 mice). ChR2-evoked inhibition decreased EPSP heights by 25.2 ± 9.0% (Fig. 5H, green) and shifted the peak of EPSPs forward 57.5 ± 26μs (Fig. 5I, green), with only a 5% decrease in EPSP half-width (Fig. 5J, green). This effect was mimicked by bath application of 25μM glycine (Fig. 5H-J, blue: *n* = 4 cells, 3 mice). Further, bath application of 1μM STN had the opposite effect, resulting in larger EPSPs, delayed peak times, and increased half-widths (Fig. 5H-J, orange: *n* = 5 cells, 4 mice). Thus, the timing of EPSP arrival may be shaped both by the release of synaptic glycine and tonically active glycine channels. Importantly, many ANFs also terminate on the octopus cell soma, where inhibition is minimal. This suggests that the octopus cell's ability to act as a coincidence detector depends on two stages of compartmentalized computations, one in the dendrite that combines excitation and inhibition to provide important information about which frequencies co-occur in a complex sound stimulus and one in the soma that is restricted by the rigid temporal summation window for coincidence detection. Together with the unique biophysical properties of the octopus cell and the dominance of low threshold, low jitter Ia ANF inputs, these combined computations can enable reliable coincidence detection and proper binding needed for perception of sound throughout the ascending auditory pathways.

Discussion

Coincidence detection plays a critical role in many cognitive and perceptual processes, from the ability to localize sound, to the binding of auditory and visual features of a common stimulus. Depending on the computation, the temporal window for integration can range widely, thereby requiring circuitry with distinct anatomical and physiological properties. Here, we describe a mechanism for coincidence detection that can detect co-occurring frequencies at multiple time scales. By mapping and selectively activating synaptic inputs onto octopus cells both *in vitro* and in computational models, we revealed that compartmentalized dendritic nonlinearities impact the temporal integration window under which somatic coincidence detection computations are made. The arrival of many small, stable excitatory inputs (Fig. 3) from low-threshold ANFs (Fig. 2) is continuous throughout an ongoing stimulus. We demonstrate that glycinergic inhibition to octopus cell dendrites (Fig.1) can shift the magnitude and timing of these ANF EPSPs as they summate in the soma (Fig. 4,5). The narrow window for coincidence detection computations allows the octopus cell to respond with temporal precision at the onset of the stimulus. We propose that, as a stimulus persists, inhibition onto octopus cell dendrites accelerates the timing of excitation as it travels along the dendrites and arrives at the soma for the final computation, thereby allowing the cell to also encode sequenced frequencies without compromising the accuracy of the onset computation.

As coincidence detectors in the auditory system, octopus cells are faced with the unusual challenge of recognizing complex sounds that include many co-occurring frequencies that also change together from the beginning to the end of the stimulus. As shown by *in vivo* recordings[5,28], octopus cells respond well to cues that include complex spectrotemporal patterns, including frequency modulated stimuli, in which octopus cells respond beyond the onset of the stimulus[28]. Given that the auditory environment is filled with overlapping sound stimuli, such responses presumably allow the octopus cell to better represent which frequencies belong to which sound. Our data further support the role of octopus cells beyond simple coincidence detectors that rely solely on the temporal summation of excitation. The results suggest that, despite high K_v and HCN conductances at rest, the addition of dendritic inhibition transforms the magnitude and timing of ANF signals as they arrive in the cell body, which may expand their response selectivity to include spectrotemporal sequence detection. Although this inhibition is difficult to detect, due largely to the unusual biophysical properties of the octopus cell, our data demonstrate that it is both present and impactful. Further, the effect is localized to the dendrite, highlighting the presence of a fundamentally different type of computation.

Octopus cell dendrites also differ in the nature of their excitation. In contrast to the soma, where frequency information is lost, ANF inputs onto the octopus cell dendrites are tonotopically organized. Previous models proposed that this organization corrects for the timing delay that is created within the cochlea, where soundwaves stimulate the base of the cochlea 1-2ms before they reach the apex[17]. In a system where submillisecond differences can matter significantly, such a delay could prevent accurate coincidence detection. Because ANFs from the base terminate distal to those from the apex, the dendrite itself can help ensure that signals from co-occurring low and high frequencies ultimately reach the soma at the same time. Our results raise the possibility that this computation is aided further by inhibition.

The presence of inhibitory inputs onto dendrites is a fundamental feature of the nervous system and, in other systems, contributes to the final computation. For example, it has been shown that direction selectivity computations in dendrites of retinal ganglion cells require excitation-inhibition interactions in dendritic compartments[63]. In pyramidal cells of the cortex and hippocampus, the spatial distribution of inhibition impacts dendritic non-linearities in a branch selective manner[64–69]. However, octopus cells do not share the same dendritic nonlinearities as neurons in the cortex and hippocampus. Because they lack mechanisms for dendritic action potentials, octopus cells can reveal subthreshold dynamics between strong sources of excitation and local inhibitory inputs before action potential generation.

Although this work uncovers a role for inhibition, our understanding of octopus cell computations is limited by the fact that we do not know what kind of information is being carried by inhibitory inputs. Although the presence of presynaptic glycinergic puncta in the octopus cell area[70–73] and glycinergic receptor expression in octopus cells[74–78] is well established, it is unknown where this glycinergic innervation comes from. Of the local neurons within the CNC that provide inhibition to the VCN, there is no evidence of connections to octopus cells from D-Stellate[50], L-Stellate[79], or tuberculoventral cells[80]. Outside of the CNC, terminal degeneration experiments in cats suggested the superior periolivary nucleus (SPON) and the ventral division of the lateral lemniscus (VNLL) as potential sources of descending inhibition to the octopus cell area[81]. Octopus cells are the main excitatory input to both the SPON[82–86] and the VNLL[19,87–91], raising the possibility of feedback inhibition from the auditory brainstem as a circuit mechanism for elongated temporal summation windows during ongoing stimuli. Although feedback inhibition is not rapid enough to prevent or alter the onset response that octopus cells are well-known for, it could limit the duration of a response or change the effective coincidence detection window. It is also possible that inhibition enables detection of gaps within an ongoing stimulus, which is an essential cue for speech intelligibility. Onset and offset inhibition have also been proposed to be a reference signal to bind or separate chunks of stimuli[92,93]. Once a source has been identified, it will be critical to examine if inhibitory inputs tonotopically match the local, narrowly-tuned dendritic ANF inputs. It is possible that frequency matched inhibition could play a role in spectral selectivity or feature extraction while broadly tuned inhibition could play a role in the reduction of depolarization block or serve as a temporal milestone that signals gaps or offsets.

As well as needing to work in multiple time scales, an effective coincidence detector in the auditory system must also function reliably across a range of sound intensities. Intensity information is encoded by the number and types of SGNs that are activated in the cochlea. The Ia, Ib, and Ic molecular subtypes defined in mouse[39,40,42] broadly correspond to the anatomically and physiologically defined subtypes described across species[41,94]. We find that the majority of inputs onto octopus cells come from Ia ANFs, which most closely correspond to the low-threshold, high-spontaneous rate population. Consistent with this interpretation, single-unit ANF recordings in cats demonstrated a bias towards low-threshold, high-spontaneous rate axon collaterals in the octopus cell area[32]. Low-threshold ANFs are also characterized by short first spike latencies and low temporal jitter. One of the hallmark features of the octopus cell is the fact that it only fires action potentials when many ANF inputs are activated within a narrow period of time. The presence of many low-threshold and temporally precise inputs on the octopus cell may help ensure that coincidence detection still works reliably for quiet sounds. Further, Ia inputs onto octopus cells show no synaptic depression, not unlike low levels of depression seen in Ia inputs to bushy cells[95]. The presence of stable ANF inputs could be beneficial for encoding sustained auditory signals. Finally, although Ia ANFs are over-represented, Ib and Ic inputs also exist. While precise, low-threshold ANF responses can be saturated by background noise such that responses to relevant stimuli are masked[37,96–98], recruitment of higher threshold ANFs at higher sound intensities may compensate for this tradeoff. Further characterization of *in vivo* octopus cell responses in complex sound environments may clarify the effect of noise on signal detection and could reveal additional features of this cell's contributions to perception of the auditory world.

Author Contributions

Conceptualization, L.J.K. and L.V.G.; Methodology, S.H.; Formal Analysis, L.J.K and S.H.; Investigation, L.J.K, S.M., and S.S.; Resources, G.F.; Writing, L.J.K, and L.V.G.; Visualization, L.J.K. and S.H.; Supervision, G.F. and L.V.G.; Funding Acquisition, L.J.K, G.F., and L.V.G.

Acknowledgements

We thank our collaborators Dr. Nace Golding (University of Texas at Austin), Dr. Matthew McGinley (Baylor College of Medicine), and Dr. Phillip Joris (KU Leuven) for helpful discussions and feedback. Sadie Quinn, Lucy Lee, and Ryan Merrow for technical assistance. Dr. Bruce Bean (Harvard Medical School) for generously providing access to electrophysiological equipment. *Slc6a5*$^{\mathrm{tm1.1(cre)Ksak}}$ mice were kindly provided by Dr. Wade Regehr (Harvard Medical School). *Ntng1*$^{\mathrm{em1(cre)Kfra}}$ mice were made and kindly provided by Dr. Fan Wang (Massachusetts Institute of Technology). *Myo15a*$^{\mathrm{tm1.1(cre)Ugds}}$ mice were kindly provided by Dr. Stefan Heller (Stanford). We thank Rigoberto Ramirez, Tenzin Paljorwa, and Edgar Ramirez for animal care support. Neurobiology Imaging Facility (NIF) for software availability. HMS Research Instrumentation Core for the design and fabrication of temperature regulation equipment. This work was supported by grants from the BRAIN Initiative 1R01NS118402 to L.V.G., the National Institute on Deafness and Other Communication Disorders 1F32DC020070 to L.J.K, the William Randolph Hearst Fund to L.J.K, and the Broad Institute's Stanley Center for Psychiatric Research to S.H. and G.F.

Declaration of Interests

The authors declare no competing interests.

Methods and Materials

Animal Use and Transgenic Mouse Lines

All procedures were approved by and conducted in accordance with Harvard Medical School Institutional Animal Care and Use Committee. Male and female mice (*Mus musculus*) were bred on a C57BL/6 background at the Harvard Center for Comparative Medicine or obtained from Jackson Laboratories (Bar Harbor, ME). Mice were housed in groups of up to five animals and maintained on a 12hr light/dark cycle. Transgenic alleles were heterozygous for each transgene for all experimental animals. Descriptions of allele combinations for all experiments can be found in Supp. Table 1.

Spiral ganglion neurons (SGNs) and their central auditory nerve fibers (ANFs) were targeted using either *Foxg1*$^{\text{tm1.1(cre)Ddmo}}$ (*Foxg1*$^{\text{Cre}}$)[99] or *Foxg1*$^{\text{Flp}}$, both of which drive robust reporter expression neurons in the auditory and vestibular ganglion[100,101] and the neocortex[102,103], but not in brainstem or midbrain neurons. *Foxg1*$^{\text{Flp}}$ mice were generated by crossing *Foxg1*$^{\text{tm1.1Fsh}}$, [104] and Tg(EIIa-cre)C5379Lmgd[105] mouse lines, then backcrossing to isolate the flp transgene and remove the cre transgene.

Inhibitory inputs to octopus cells were targeted with *Slc6a5*$^{\text{tm1.1(cre)Ksak}}$ mice (*Glyt2*$^{\text{Cre}}$)[106].

Octopus cells were sparsely labeled with the Tg(Thy1-YFP)HJrs (Thy1) mouse line[107]. This line labels ~0-15 octopus cells amongst other neurons throughout the brain.

Ib/c SGNs were targeted using the *Ntng1*$^{\text{em1(cre)Kfra}}$ (*Ntng1*$^{\text{Cre}}$) mouse line, which drives expression in neurons throughout the nervous system (Supp. Fig. 1F) and disrupts expression of the endogenous allele[43]. Auditory brainstem responses in adult *Ntng1*$^{\text{Cre/+}}$ mice are normal. Ic SGNs were sparsely targeted with the *Myo15a*$^{\text{tm1.1(cre)Ugds}}$ (*Myo15*$^{\text{iCre}}$) mouse line[108].

Fluorescent reporters included *Gt(ROSA)26Sor*$^{\text{tm14(CAG-tdTomato)}}$ (Ai14, tdTom; Jax strain 007914)[109], *Gt(Rosa)26Sor*$^{\text{tm34.1(CAG-Syp/tdTomato)}}$ (Ai34, syp; Jax 012570), and *Gt(Rosa)26Sor*$^{\text{tm1.2(CAG-EGFP)Fsh}}$ (RCE:FRT, EYFP)[110]. We also used *Gt(Rosa)26Sor*$^{\text{tm32(CAG-COP4*H134R.EYFP)}}$ (Ai32, ChR2; Jax 012569)[111] to drive synaptic activity in *in vitro* slice experiments.

Histology and Reconstructions

For immunohistochemical labeling, mice were deeply anesthetized with isoflurane and transcardially perfused with 15mL of 4% paraformaldehyde (PFA) in 0.1M phosphate-buffered saline (PBS) using a peristaltic pump (Gilson). Whole skulls containing brain and cochlea were immediately transferred to 20mL of 4% PFA and post-fixed overnight at 4°C. Fixed brains and cochlea were removed from the skulls and washed with 0.1M PBS.

Brain Sections

Brains were collected from mice of both sexes, aged 28-38 days, and embedded in gelatin-albumin hardened with 5% glutaraldehyde and 37% PFA[112]. Sections were cut at 35, 65, or 100μm with a vibrating microtome (Leica VT1000S) and free-floating tissue was collected in 0.1M PBS. For sections less than 65μm, tissue was permeabilized and nonspecific staining was blocked in a solution of 0.2% Triton X-100 and 5% normal donkey serum (NDS) in 0.1M PBS for 1 hour. After blocking, tissue was treated with primary antibody in a solution containing 0.2% Triton X-100 and 5% NDS in PBS for 1-2 nights at room temperature. Primary antibodies used were: chicken anti-GFP (1:1000, cat#GFP-1020, Aves), rabbit anti-RFP (1:1000, item#600-401-379-RTU, Rockland Immunochemicals), goat anti-calretinin (1:1000, SKU: CG1, Swant), and guinea pig anti-VGLUT1 (1:500, cat#135304, Synaptic Systems). Sections were washed in 0.1M PBS then incubated in a secondary antibody solution (1:1000) containing 0.2% Triton X-100 and 5% NDS for 2-3hrs at room temperature. Tissue sections were mounted on charged slides and coverslipped (Vectashield Hardset Antifade Mounting Medium with DAPI), and imaged using a Zeiss Observer.Z1 confocal microscope.

For 100µm sections, tissue was washed in CUBIC-1A solution for 1hr for strong permeabilization and delipidization[113,114]. Tissue was then further permeabilized and nonspecific staining was blocked in a solution of 0.2% Triton X-100 and 5% NDS in 0.1M PBS for 1hr. After blocking, tissue was treated with primary antibody in a solution containing 0.2% Triton X-100 and 5% NDS in PBS for 4 nights at 37°C. Primary antibodies used were: chicken anti-GFP (1:1000, cat#GFP-1020, Aves), and rabbit anti-RFP (1:1000, item# 600-401-379-RTU, Rockland Immunochemicals). Sections were then incubated in a secondary antibody solution (1:400) containing 0.2% Triton X-100 and 5% NDS for 4 nights at 37°C. Tissue sections were pre-incubated in CUBIC2 solution, then temporarily mounted on uncharged slides with CUBIC2 solution for immediate imaging using a Zeiss Observer.Z1 confocal microscope.

3D Reconstructions

Octopus cells and synaptic puncta were reconstructed in Imaris (Oxford Instruments). Thy1 signal from the target octopus cell was used to generate a surface reconstruction and mask YFP and syp signal. Dendrites were reconstructed using the masked YFP signal and separated into 10µm increments. Masked syp puncta were marked and localized to a 10µm increment of the dendritic tree. Synapse counts, dendrite metrics, and masked channels were exported to Excel (Microsoft) for further analysis.

Cochlea Sections

Cochlea were collected from mice of both sexes, aged 28-42 days. The bony labyrinth of the inner ear was decalcified in 0.5M ethylenediamine tetraacetic acid (EDTA) for 3 nights at 4°C and embedded in gelatin-albumin hardened with 5% glutaraldehyde and 37% PFA. Sections were cut at 65µm with a vibrating microtome (Leica VT1000S) and free-floating tissue was collected in 0.1M PBS. Sections were washed in CUBIC-1A solution for 1hr for strong permeabilization and delipidization. Tissue was further permeabilized and nonspecific staining was blocked in a solution of 0.2% Triton X-100 and 5% NDS in 0.1M PBS for 1hr. After blocking, tissue was treated with primary antibody in a solution containing 0.2% Triton X-100 and 5% NDS in PBS for 2 nights at room temperature. Primary antibodies used were: chicken anti-GFP (1:1000, cat#GFP-1020, Aves), rabbit anti-RFP (1:1000, item#600-401-379-RTU, Rockland Immunochemicals), goat anti-calretinin (1:1000, SKU: CG1, Swant). Sections were then incubated in a secondary antibody solution (1:500) containing 0.2% Triton X-100 and 5% normal goat serum for 2-3hrs at room temperature. Tissue sections were mounted on charged slides, coverslipped (Vectashield Hardset Antifade Mounting Medium with DAPI), and imaged using a Zeiss Observer.Z1 confocal microscope.

Acute Slice Electrophysiology

Data were obtained from mice of both sexes, aged 24-47 days. Mice were deeply anesthetized with isoflurane and perfused transcardially with 3mL of 35°C artificial cerebral spinal fluid (ACSF; 125mM NaCl, 25mM glucose, 25mM $NaHCO_3$, 2.5mM KCl, 1.25mM NaH_2PO_4, 1.4mM $CaCl_2$, and 1.6mM $MgSO_4$, pH adjusted to 7.45 with NaOH). For high calcium concentration experiments presented in Fig. 3C, ACSF contained 125mM NaCl, 25mM glucose, 25mM $NaHCO_3$, 2.5mM KCl, 1.25mM NaH_2PO_4, 2.4mM $CaCl_2$, and 1.3mM $MgSO_4$. Mice were rapidly decapitated and the brain was removed and immediately submerged in ACSF. Brains were bisected and 250µm slices were prepared in the sagittal plane with a vibrating microtome (Leica VT1200S; Leica Systems). Prepared slices were incubated for 30min at 35°C, then allowed to recover at room temperature for at least 30min. ACSF was continuously bubbled with 95% O_2/5% CO_2.

Whole-cell recordings were conducted at 35°C using a Multiclamp 700B (Molecular Devices) in current-clamp mode with experimenter adjusted and maintained bridge balance and capacitance compensation. Data were low pass filtered at 5kHz, digitized at 83–100kHz, and acquired using pClamp9 (Molecular Devices). Neurons were visualized using infrared Dodt gradient contrast (Zeiss Examiner.D1; Zeiss Axiocam 305 mono). Glass recording electrodes (3–7MΩ) were wrapped in parafilm to reduce capacitance and filled with an intracellular solution containing 115mM K-gluconate, 4.42mM KCl, 0.5mM EGTA, 10mM HEPES, 10mM Na_2Phosphocreatine, 4mM MgATP, 0.3mM NaGTP, and 0.1% biocytin, osmolality adjusted to 300mmol/kg with sucrose, pH adjusted to 7.30 with KOH. All membrane potentials are corrected for a 11mV junction potential.

For optogenetic activation, full-field 470nm blue light was presented through a 20x immersion objective (Zeiss Examiner.D1). Onset, duration, and intensity of light was controlled by a Colibri5 LED Light Source (Zeiss). For electrical stimulation, glass stimulating electrodes were placed in the auditory nerve root and 20μs current pulses were generated with a DS3 current stimulator (Digitimer).

Analysis and Statistical Tests

Cell counts and habenula measurements were performed in ImageJ/FIJI software (National Institutes of Health). Electrophysiology data were analyzed using custom scripts and NeuroMatic analysis routines[115] in Igor Pro (Wavemetrics).

For data with equal variance (Levene's test), one-way ANOVAs with Tukey's HSD post hoc test were used where appropriate to determine statistical significance. For data with non-homogenous variances, one-way ANOVAs with a Welch F test were used with a Tukey's HSD post hoc test. Errors and error bars report standard deviation (SD) or standard error of the mean (SEM) as noted in figure legends and throughout the text.

Computational Modelling

Computer simulations were performed using the NEURON 8.2 simulation environment[116], with an integration time constant of 25μs. The morphology of the octopus neuron was obtained from McGinley et al., 2012. The active and passive properties of the model were optimized to match the experimental recordings. We set the passive parameters as follows: internal or axial resistance (R_i or R_a) to 150Ω.cm, membrane resistance (R_m) to 5KΩ.cm^2, capacitance (C_m) to 0.9μF/Cm^2 and resting membrane potential (V_m) to -65mV. We included the following ion-channel conductances in our morphologically realistic octopus neuron model: Fast Na^+ ($\bar{g}_{NA}$), low-voltage activated K^+ ($\bar{g}_{KLT}$), high threshold K^+ ($\bar{g}_{KHT}$), fast transient K^+ ($\bar{g}_{KA}$), hyperpolarization-activated cyclic nucleotide-gated HCN ($\bar{g}_h$), leak K^+ ($\bar{g}_{leak}$). The kinetics of all the active ion-channel conductances were obtained from Manis and Campagnola, 2018 and the maximal conductance was optimized to match experimental data. We introduced a scaling factor (scl) to scale the maximal conductance to match the sag and input resistance of the experimental recordings (Supp. Fig. 4). Reversal potentials for HCN, Na^+ and K^+ respectively were (in mV), E_h= -38, E_{Na}= 50 and E_K= -70. Excitatory AMPA synaptic conductance and Inhibitory glycine synaptic conductance were introduced in the proximal and distal dendrites to test the impact of dendritic inhibition on the EPSP height and peak time. The rise and decay time of AMPA and glycine conductance were set to 0.3ms and 3ms respectively, to mimic the fast synaptic transients observed in octopus cells. The reversal potential of AMPA and glycine conductance was set to 0 and -80mV respectively.

References

1. Shamma, S.A., Elhilali, M., and Micheyl, C. (2011). Temporal coherence and attention in auditory scene analysis. Trends Neurosci. *34*, 114–123. 10.1016/j.tins.2010.11.002.
2. Osen, K.K. (1969). The intrinsic organization of the cochlear nuclei in the cat. Acta Otolaryngol. (Stockh.) *67*, 352–359. 10.3109/00016486909125462.
3. Osen, K.K. (1969). Cytoarchitecture of the cochlear nuclei in the cat. J. Comp. Neurol. *136*, 453–483. 10.1002/cne.901360407.
4. Godfrey, D.A., Kiang, N.Y.S., and Norris, B.E. (1975). Single unit activity in the posteroventral cochlear nucleus of the cat. J. Comp. Neurol. *162*, 247–268. 10.1002/cne.901620206.
5. Recio-Spinoso, A., and Rhode, W.S. (2020). Information Processing by Onset Neurons in the Cat Auditory Brainstem. JARO - J. Assoc. Res. Otolaryngol. *21*, 201–224. 10.1007/s10162-020-00757-0.
6. Rhode, W.S., Smith, P.H., and Oertel, D. (1983). Physiological response properties of cells labeled intracellularly with horseradish peroxidase in cat dorsal cochlear nucleus. J. Comp. Neurol. *213*, 426–447. 10.1002/cne.902130407.
7. Ritz, L.A., and Brownell, W.E. (1982). Single unit analysis of the posteroventral cochlear nucleus of the decerebrate cat. Neuroscience *7*, 1995–2010. 10.1016/0306-4522(82)90013-6.
8. Bal, R., and Oertel, D. (2000). Hyperpolarization-activated, mixed-cation current (I(h)) in octopus cells of the mammalian cochlear nucleus. J. Neurophysiol. *84*, 806–817. 10.1152/jn.2000.84.2.806.
9. Bal, R., and Oertel, D. (2001). Potassium currents in octopus cells of the mammalian cochlear nucleus. J. Neurophysiol. *86*, 2299–2311. 10.1152/jn.2001.86.5.2299.
10. Cao, X.J., and Oertel, D. (2017). Genetic perturbations suggest a role of the resting potential in regulating the expression of the ion channels of the KCNA and HCN families in octopus cells of the ventral cochlear nucleus. Hear. Res. *345*, 57–68. 10.1016/j.heares.2017.01.001.
11. Golding, N.L., Robertson, D., and Oertel, D. (1995). Recordings from slices indicate that octopus cells of the cochlear nucleus detect coincident firing of auditory nerve fibers with temporal precision. J. Neurosci. *15*, 3138–3153. 10.1523/jneurosci.15-04-03138.1995.
12. Golding, N.L., Ferragamo, M.J., and Oertel, D. (1999). Role of intrinsic conductances underlying responses to transients in octopus cells of the cochlear nucleus. J. Neurosci. *19*, 2897–2905. 10.1523/jneurosci.19-08-02897.1999.
13. Golding, N.L., and Oertel, D. (2012). Synaptic integration in dendrites: Exceptional need for speed. J. Physiol. *590*, 5563–5569. 10.1113/jphysiol.2012.229328.
14. Manis, P.B., and Marx, S.O. (1991). Outward currents in isolated ventral cochlear nucleus neurons. J. Neurosci. *11*, 2865–2880. 10.1523/jneurosci.11-09-02865.1991.
15. Oertel, D. (1983). Synaptic responses and electrical properties of cells in brain slices of the mouse anteroventral cochlear nucleus. J. Neurosci. *3*, 2043–2053. 10.1523/jneurosci.03-10-02043.1983.
16. McGinley, M.J. (2014). Rapid Integration Across Tonotopy by Individual Auditory Brainstem Octopus Cells. In The Computing Dendrite, From Structure to Function, H. Cuntz, M. W. H. Remme, and B. Torben-Nielsen, eds., pp. 223–243. 10.1007/978-1-4614-8094-5_14.
17. McGinley, M.J., Liberman, M.C., Bal, R., and Oertel, D. (2012). Generating Synchrony from the Asynchronous: Compensation for Cochlear Traveling Wave Delays by the Dendrites of Individual Brainstem Neurons. J. Neurosci. *32*, 9301–9311. 10.1523/jneurosci.0272-12.2012.
18. Lu, H.W., Smith, P.H., and Joris, P.X. (2018). Submillisecond monaural coincidence detection by octopus cells. Acta Acust. United Acust. *104*, 852–855. 10.3813/AAA.919238.
19. Smith, P.H., Massie, A., and Joris, P.X. (2005). Acoustic stria: Anatomy of physiologically characterized cells and their axonal projection patterns. J. Comp. Neurol. *482*, 349–371. 10.1002/cne.20407.
20. Smith, P.H., Joris, P.X., Banks, M.I., and Yin, T.C.T. (1993). Responses of Cochlear Nucleus Cells and Projections of their Axons. In The Mammalian Cochlear Nuclei: Organization and Function NATO ASI series., M. A. Merchán, J. M. Juiz, D. A. Godfrey, and E. Mugnaini, eds. (Springer US), pp. 349–360. 10.1007/978-1-4615-2932-3_27.
21. Cai, Y., McGee, J., and Walsh, E.J. (2000). Contributions of Ion Conductances to the Onset Responses of Octopus Cells in the Ventral Cochlear Nucleus: Simulation Results. J. Neurophysiol. *83*, 301–314. 10.1152/jn.2000.83.1.301.
22. Cai, Y., Walsh, E.J., and McGee, J. (1997). Mechanisms of Onset Responses in Octopus Cells of the Cochlear Nucleus: Implications of a Model. J. Neurophysiol. *78*, 872–883. 10.1152/jn.1997.78.2.872.

23. Kipke, D.R., and Levy, K.L. (1997). Sensitivity of the cochlear nucleus octopus cell to synaptic and membrane properties: A modeling study. J. Acoust. Soc. Am. *102*, 403–412. 10.1121/1.419762.
24. Levy, K.L., and Kipke, D.R. (1998). Mechanisms of the cochlear nucleus octopus cell's onset response: Synaptic effectiveness and threshold. J. Acoust. Soc. Am. *103*, 1940–1950. 10.1121/1.421346.
25. Levy, K.L., and Kipke, D.R. (1997). A computational model of the cochlear nucleus octopus cell. J. Acoust. Soc. Am. *102*, 391–402. 10.1121/1.419761.
26. Rebhan, M., and Leibold, C. (2021). A phenomenological spiking model for octopus cells in the posterior–ventral cochlear nucleus. Biol. Cybern. *115*, 331–341. 10.1007/s00422-021-00881-x.
27. Spencer, M., Grayden, D., Bruce, I., Meffin, H., and Burkitt, A. (2012). An investigation of dendritic delay in octopus cells of the mammalian cochlear nucleus. Front. Comput. Neurosci. *6*. https://doi.org/10.3389/fncom.2012.00083.
28. Lu, H.-W., Smith, P.H., and Joris, P.X. (2022). Mammalian octopus cells are direction selective to frequency sweeps by excitatory synaptic sequence detection. Proc. Natl. Acad. Sci. *119*, e2203748119. 10.1073/pnas.2203748119.
29. Gómez-Nieto, R., and Rubio, M.E. (2009). A bushy cell network in the rat ventral cochlear nucleus. J. Comp. Neurol. *516*, 241–263. 10.1002/cne.22139.
30. Zhou, J., Nannapaneni, N., and Shore, S. (2007). Vessicular glutamate transporters 1 and 2 are differentially associated with auditory nerve and spinal trigeminal inputs to the cochlear nucleus. J. Comp. Neurol. *500*, 777–787. 10.1002/cne.21208.
31. Liberman, M.C. (1991). Central projections of auditory-nerve fibers of differing spontaneous rate. I. Anteroventral cochlear nucleus. J. Comp. Neurol. *313*, 240–258. 10.1002/cne.903130205.
32. Liberman, M.C. (1993). Central projections of auditory nerve fibers of differing spontaneous rate, II: Posteroventral and dorsal cochlear nuclei. J. Comp. Neurol. *327*, 17–36. 10.1002/cne.903270103.
33. Rouiller, E.M., Cronin-Schreiber, R., Fekete, D.M., and Ryugo, D.K. (1986). The central projections of intracellularly labeled auditory nerve fibers in cats: an analysis of terminal morphology. J. Comp. Neurol. *249*, 261–278. 10.1002/cne.902490210.
34. Rouiller, E.M., and Ryugo, D.K. (1984). Intracellular marking of physiologically characterized cells in the ventral cochlear nucleus of the cat. J. Comp. Neurol. *225*, 167–186. 10.1002/cne.902250203.
35. Tsuji, J., and Liberman, M.C. (1997). Intracellular labeling of auditory nerve fibers in guinea pig: central and peripheral projections. J. Comp. Neurol. *381*, 188–202. 10.1002/(SICI)1096-9861(19970505)381:2<188::AID-CNE6>3.0.CO;2-#.
36. Liberman, L.D., Wang, H., and Liberman, M.C. (2011). Opposing Gradients of Ribbon Size and AMPA Receptor Expression Underlie Sensitivity Differences among Cochlear-Nerve/Hair-Cell Synapses. J. Neurosci. *31*, 801–808. 10.1523/JNEUROSCI.3389-10.2011.
37. Liberman, M.C. (1978). Auditory-nerve response from cats raised in a low-noise chamber. J. Acoust. Soc. Am. *63*, 442–455. 10.1121/1.381736.
38. Liberman, M.C. (1982). Single-neuron labeling in the cat auditory nerve. Science *216*, 1239–1241. 10.1126/science.7079757.
39. Petitpré, C., Wu, H., Sharma, A., Tokarska, A., Fontanet, P., Wang, Y., Helmbacher, F., Yackle, K., Silberberg, G., Hadjab, S., et al. (2018). Neuronal heterogeneity and stereotyped connectivity in the auditory afferent system. Nat. Commun. *9*, 3691. 10.1038/s41467-018-06033-3.
40. Shrestha, B.R., Chia, C., Wu, L., Kujawa, S.G., Liberman, M.C., and Goodrich, L.V. (2018). Sensory Neuron Diversity in the Inner Ear Is Shaped by Activity. Cell *174*, 1229-1246.e17. 10.1016/j.cell.2018.07.007.
41. Siebald, C., Vincent, P.F.Y., Bottom, R.T., Sun, S., Reijntjes, D.O.J., Manca, M., Glowatzki, E., and Müller, U. (2023). Molecular signatures define subtypes of auditory afferents with distinct peripheral projection patterns and physiological properties. Proc. Natl. Acad. Sci. U. S. A. *120*, e2217033120. 10.1073/pnas.2217033120.
42. Sun, S., Babola, T., Pregernig, G., So, K.S., Nguyen, M., Su, S.-S.M., Palermo, A.T., Bergles, D.E., Burns, J.C., and Müller, U. (2018). Hair Cell Mechanotransduction Regulates Spontaneous Activity and Spiral Ganglion Subtype Specification in the Auditory System. Cell *174*, 1247-1263.e15. 10.1016/j.cell.2018.07.008.

43. Bolding, K.A., Nagappan, S., Han, B.-X., Wang, F., and Franks, K.M. (2020). Recurrent circuitry is required to stabilize piriform cortex odor representations across brain states. eLife *9*, e53125. 10.7554/eLife.53125.
44. Muniak, M.A., Rivas, A., Montey, K.L., May, B.J., Francis, H.W., and Ryugo, D.K. (2013). 3D model of frequency representation in the cochlear nucleus of the CBA/J mouse. J. Comp. Neurol. *521*, 1510–1532. 10.1002/cne.23238.
45. Cao, X.J., and Oertel, D. (2010). Auditory nerve fibers excite targets through synapses that vary in convergence, strength, and short-term plasticity. J. Neurophysiol. *104*, 2308–2320. 10.1152/jn.00451.2010.
46. Yang, H., and Xu-Friedman, M.A. (2009). Impact of Synaptic Depression on Spike Timing at the Endbulb of Held. J. Neurophysiol. *102*, 1699–1710. 10.1152/jn.00072.2009.
47. Cao, X.-J., McGinley, M.J., and Oertel, D. (2008). Connections and synaptic function in the posteroventral cochlear nucleus of deaf jerker mice. J. Comp. Neurol. *510*, 297–308. 10.1002/cne.21788.
48. Oertel, D., Bal, R., Gardner, S., and PH (2000). Detection of synchrony in the activity of auditory nerve fibers by octopus cells of the mammalian cochlear nucleus. Proc. Of *97*, 11773–11779. 10.1073/pnas.97.22.11773 97/22/11773.
49. Bal, R., Baydas, G., and Naziroglu, M. (2009). Electrophysiological properties of ventral cochlear nucleus neurons of the dog. Hear. Res. *256*, 93–103. 10.1016/j.heares.2009.07.004.
50. Oertel, D., Wu, S.H., Garb, M.W., and Dizack, C. (1990). Morphology and physiology of cells in slice preparations of the posteroventral cochlear nucleus of mice. J. Comp. Neurol. *295*, 136–154. 10.1002/cne.902950112.
51. Lynch, J.W., Rajendra, S., Barry, P.H., and Schofield, P.R. (1995). Mutations Affecting the Glycine Receptor Agonist Transduction Mechanism Convert the Competitive Antagonist, Picrotoxin, into an Allosteric Potentiator. J. Biol. Chem. *270*, 13799–13806. 10.1074/jbc.270.23.13799.
52. Pribilla, I., Takagi, T., Langosch, D., Bormann, J., and Betz, H. (1992). The atypical M2 segment of the beta subunit confers picrotoxinin resistance to inhibitory glycine receptor channels. EMBO J. *11*, 4305–4311. 10.1002/j.1460-2075.1992.tb05529.x.
53. Wang, D.-S., Mangin, J.-M., Moonen, G., Rigo, J.-M., and Legendre, P. (2006). Mechanisms for Picrotoxin Block of α2 Homomeric Glycine Receptors. J. Biol. Chem. *281*, 3841–3855. 10.1074/jbc.M511022200.
54. Hruskova, B., Trojanova, J., Kulik, A., Kralikova, M., Pysanenko, K., Bures, Z., Syka, J., Trussell, L.O., and Turecek, R. (2012). Differential Distribution of Glycine Receptor Subtypes at the Rat Calyx of Held Synapse. J. Neurosci. *32*, 17012–17024. 10.1523/JNEUROSCI.1547-12.2012.
55. Zhang, X.-B., Sun, G.-C., Liu, L.-Y., Yu, F., and Xu, T.-L. (2008). Alpha2 subunit specificity of cyclothiazide inhibition on glycine receptors. Mol. Pharmacol. *73*, 1195–1202. 10.1124/mol.107.042655.
56. Dutertre, S., Becker, C.-M., and Betz, H. (2012). Inhibitory Glycine Receptors: An Update *. J. Biol. Chem. *287*, 40216–40223. 10.1074/jbc.R112.408229.
57. Lynch, J.W. (2009). Native glycine receptor subtypes and their physiological roles. Neuropharmacology *56*, 303–309. 10.1016/j.neuropharm.2008.07.034.
58. Veruki, M.L., Gill, S.B., and Hartveit, E. (2007). Spontaneous IPSCs and glycine receptors with slow kinetics in wide-field amacrine cells in the mature rat retina. J. Physiol. *581*, 203–219. 10.1113/jphysiol.2006.127316.
59. Manis, P.B., and Campagnola, L. (2018). A biophysical modelling platform of the cochlear nucleus and other auditory circuits: From channels to networks. Hear. Res. *360*, 76–91. 10.1016/j.heares.2017.12.017.
60. Jackman, S.L., Beneduce, B.M., Drew, I.R., and Regehr, W.G. (2014). Achieving High-Frequency Optical Control of Synaptic Transmission. J. Neurosci. *34*, 7704–7714. 10.1523/jneurosci.4694-13.2014.
61. Mathie, A., Wooltorton, J.R.A., and Watkins, C.S. (1998). Voltage-activated potassium channels in mammalian neurons and their block by novel pharmacological agents. Gen. Pharmacol. Vasc. Syst. *30*, 13–24. 10.1016/S0306-3623(97)00034-7.
62. Koch, C., Poggio, T., and Torre, V. (1983). Nonlinear interactions in a dendritic tree: localization, timing, and role in information processing. Proc. Natl. Acad. Sci. U. S. A. *80*, 2799–2802.

63. Stasheff, S.F., and Masland, R.H. (2002). Functional Inhibition in Direction-Selective Retinal Ganglion Cells: Spatiotemporal Extent and Intralaminar Interactions. J. Neurophysiol. *88*, 1026–1039. 10.1152/jn.2002.88.2.1026.
64. Bloss, E.B., Cembrowski, M.S., Karsh, B., Colonell, J., Fetter, R.D., and Spruston, N. (2016). Structured Dendritic Inhibition Supports Branch-Selective Integration in CA1 Pyramidal Cells. Neuron *89*, 1016–1030. 10.1016/j.neuron.2016.01.029.
65. Gidon, A., and Segev, I. (2012). Principles governing the operation of synaptic inhibition in dendrites. Neuron *75*, 330–341. 10.1016/j.neuron.2012.05.015.
66. Hao, J., Wang, X., Dan, Y., Poo, M., and Zhang, X. (2009). An arithmetic rule for spatial summation of excitatory and inhibitory inputs in pyramidal neurons. Proc. Natl. Acad. Sci. U. S. A. *106*, 21906–21911. 10.1073/pnas.0912022106.
67. Iascone, D.M., Li, Y., Sümbül, U., Doron, M., Chen, H., Andreu, V., Goudy, F., Blockus, H., Abbott, L.F., Segev, I., et al. (2020). Whole-Neuron Synaptic Mapping Reveals Spatially Precise Excitatory/Inhibitory Balance Limiting Dendritic and Somatic Spiking. Neuron *106*, 566-578.e8. 10.1016/j.neuron.2020.02.015.
68. Jadi, M., Polsky, A., Schiller, J., and Mel, B.W. (2012). Location-Dependent Effects of Inhibition on Local Spiking in Pyramidal Neuron Dendrites. PLOS Comput. Biol. *8*, e1002550. 10.1371/journal.pcbi.1002550.
69. Lovett-Barron, M., Turi, G.F., Kaifosh, P., Lee, P.H., Bolze, F., Sun, X.-H., Nicoud, J.-F., Zemelman, B.V., Sternson, S.M., and Losonczy, A. (2012). Regulation of neuronal input transformations by tunable dendritic inhibition. Nat. Neurosci. *15*, 423–430. 10.1038/nn.3024.
70. Juiz, J.M., Helfert, R.H., Bonneau, J.M., Wenthold, R.J., and Altschuler, R.A. (1996). Three classes of inhibitory amino acid terminals in the cochlear nucleus of the guinea pig. J. Comp. Neurol. *373*, 11–26. 10.1002/(SICI)1096-9861(19960909)373:1<11::AID-CNE2>3.0.CO;2-G.
71. Kemmer, M., and Vater, M. (1997). The distribution of GABA and glycine immunostaining in the cochlear nucleus of the mustached bat (Pteronotus parnellii). Cell Tissue Res. *287*, 487–506. 10.1007/s004410050773.
72. Kolston, J., Osen, K.K., Hackney, C.M., Ottersen, O.P., and Storm-Mathisen, J. (1992). An atlas of glycine- and GABA-like immunoreactivity and colocalization in the cochlear nuclear complex of the guinea pig. Anat. Embryol. (Berl.) *186*, 443–465.
73. Moore, J.K., Osen, K.K., Storm-Mathisen, J., and Ottersen, O.P. (1996). gamma-Aminobutyric acid and glycine in the baboon cochlear nuclei: an immunocytochemical colocalization study with reference to interspecies differences in inhibitory systems. J. Comp. Neurol. *369*, 497–519. 10.1002/(SICI)1096-9861(19960610)369:4<497::AID-CNE2>3.0.CO;2-#.
74. Adams, J.C., and Mugnaini, E. (1987). Patterns of glutamate decarboxylase immunostaining in the feline cochlear nuclear complex studied with silver enhancement and electron microscopy. J. Comp. Neurol. *262*, 375–401. 10.1002/cne.902620305.
75. Friauf, E., Hammerschmidt, B., and Kirsch, J. (1997). Development of adult-type inhibitory glycine receptors in the central auditory system of rats. J. Comp. Neurol. *385*, 117–134. 10.1002/(sici)1096-9861(19970818)385:1<117::aid-cne7>3.0.co;2-5.
76. Sato, K., Kuriyama, H., and Altschuler, R.A. (2000). Expression of glycine receptor subunit mRNAs in the rat cochlear nucleus. Hear. Res. *144*, 47–52. 10.1016/s0378-5955(00)00044-7.
77. Schofield, B.R., and Cant, N.B. (1996). Origins and targets of commissural connections between the cochlear nuclei in guinea pigs. J. Comp. Neurol. *375*, 128–146. 10.1002/(SICI)1096-9861(19961104)375:1<128::AID-CNE8>3.0.CO;2-5.
78. Thompson, G.C., Cortez, A.M., and Lam, D.M.K. (1985). Localization of GABA immunoreactivity in the auditory brainstem of guinea pigs. Brain Res. *339*, 119–122. 10.1016/0006-8993(85)90628-6.
79. Ngodup, T., Romero, G.E., and Trussell, L.O. (2020). Identification of an inhibitory neuron subtype, the L-stellate cell of the cochlear nucleus. eLife *9*, e54350. 10.7554/eLife.54350.
80. Wickesberg, R.E., Whitlon, D., and Oertel, D. (1991). Tuberculoventral Neurons Project to the Multipolar Cell Area But Not to the Octopus Cell Area of the Posteroventral Cochlear Nucleus. *313*, 457–468. 10.1002/cne.903130306.
81. Kane, E.S. (1977). Descending inputs to octopus cell area of the cat cochlear nucleus: An electron microscopic study. J. Comp. Neurol. *173*, 337–354. 10.1002/cne.901730209.

82. Felix II, R.A., Gourévitch, B., Gómez-Álvarez, M., Leijon, S.C.M., Saldaña, E., and Magnusson, A.K. (2017). Octopus Cells in the Posteroventral Cochlear Nucleus Provide the Main Excitatory Input to the Superior Paraolivary Nucleus. Front. Neural Circuits *11*.
83. Friauf, E., and Ostwald, J. (1988). Divergent projections of physiologically characterized rat ventral cochlear nucleus neurons as shown by intra-axonal injection of horseradish peroxidase. Exp. Brain Res. *73*, 263–284. 10.1007/BF00248219.
84. Schofield, B.R. (1995). Projections from the cochlear nucleus to the superior paraolivary nucleus in guinea pigs. J. Comp. Neurol. *360*, 135–149. 10.1002/cne.903600110.
85. Thompson, A.M., and Thompson, G.C. (1991). Projections from the posteroventral cochlear nucleus to the superior olivary complex in guinea pig: Light and em observations with the PHA-L method. J. Comp. Neurol. *311*, 495–508. 10.1002/cne.903110405.
86. Zook, J.M., and Casseday, J.H. (1985). Projections from the cochlear nuclei in the mustache bat, Pteronotus parnellii. J. Comp. Neurol. *237*, 307–324. 10.1002/cne.902370303.
87. Adams, J.C. (1997). Projections from octopus cells of the posteroventral cochlear nucleus to the ventral nucleus of the lateral lemniscus in cat and human. Audit. Neurosci. *3*, 335–350.
88. Berger, C., Meyer, E.M.M., Ammer, J.J., and Felmy, F. (2014). Large Somatic Synapses on Neurons in the Ventral Lateral Lemniscus Work in Pairs. J. Neurosci. *34*, 3237–3246. 10.1523/JNEUROSCI.3664-13.2014.
89. Nayagam, D.A.X., Clarey, J.C., and Paolini, A.G. (2005). Powerful, Onset Inhibition in the Ventral Nucleus of the Lateral Lemniscus. J. Neurophysiol. *94*, 1651–1654. 10.1152/jn.00167.2005.
90. Schofield, B.R., and Cant, N.B. (1997). Ventral nucleus of the lateral lemniscus in guinea pigs: Cytoarchitecture and inputs from the cochlear nucleus. J. Comp. Neurol. *379*, 363–385. 10.1002/(SICI)1096-9861(19970317)379:3<363::AID-CNE4>3.0.CO;2-1.
91. Vater, M., and Feng, A.S. (1990). Functional organization of ascending and descending connections of the cochlear nucleus of horseshoe bats. J. Comp. Neurol. *292*, 373–395. 10.1002/cne.902920305.
92. Nayagam, D.A.X., Clarey, J.C., and Paolini, A.G. (2006). Intracellular responses and morphology of rat ventral complex of the lateral lemniscus neurons in vivo. J. Comp. Neurol. *498*, 295–315. 10.1002/cne.21058.
93. Recio-Spinoso, A., and Joris, P.X. (2014). Temporal properties of responses to sound in the ventral nucleus of the lateral lemniscus. J. Neurophysiol. *111*, 817–835. 10.1152/jn.00971.2011.
94. Moser, T., Karagulyan, N., Neef, J., and Jaime Tobón, L.M. (2023). Diversity matters — extending sound intensity coding by inner hair cells via heterogeneous synapses. EMBO J. *42*, e114587. 10.15252/embj.2023114587.
95. Zhang, C., Wang, M., Lin, S., and Xie, R. (2022). Calretinin-Expressing Synapses Show Improved Synaptic Efficacy with Reduced Asynchronous Release during High-Rate Activity. J. Neurosci. *42*, 2729–2742. 10.1523/JNEUROSCI.1773-21.2022.
96. Bourien, J., Tang, Y., Batrel, C., Huet, A., Lenoir, M., Ladrech, S., Desmadryl, G., Nouvian, R., Puel, J.-L., and Wang, J. (2014). Contribution of auditory nerve fibers to compound action potential of the auditory nerve. J. Neurophysiol. *112*, 1025–1039. 10.1152/jn.00738.2013.
97. Costalupes, J.A., Young, E.D., and Gibson, D.J. (1984). Effects of continuous noise backgrounds on rate response of auditory nerve fibers in cat. J. Neurophysiol. *51*, 1326–1344. 10.1152/jn.1984.51.6.1326.
98. Huet, A., Batrel, C., Tang, Y., Desmadryl, G., Wang, J., Puel, J.-L., and Bourien, J. (2016). Sound coding in the auditory nerve of gerbils. Hear. Res. *338*, 32–39. 10.1016/j.heares.2016.05.006.
99. Kawaguchi, D., Sahara, S., Zembrzycki, A., and O'Leary, D.D.M. (2016). Generation and analysis of an improved Foxg1-IRES-Cre driver mouse line. Dev. Biol. *412*, 139–147. 10.1016/j.ydbio.2016.02.011.
100. Hatini, V., Ye, X., Balas, G., and Lai, E. (1999). Dynamics of placodal lineage development revealed by targeted transgene expression. Dev. Dyn. *215*, 332–343. 10.1002/(SICI)1097-0177(199908)215:4<332::AID-AJA5>3.0.CO;2-R.
101. Pauley, S., Lai, E., and Fritzsch, B. (2006). Foxg1 Is Required for Morphogenesis and Histogenesis of the Mammalian Inner Ear. Dev. Dyn. Off. Publ. Am. Assoc. Anat. *235*, 2470–2482. 10.1002/dvdy.20839.
102. Hanashima, C., Shen, L., Li, S.C., and Lai, E. (2002). Brain Factor-1 Controls the Proliferation and Differentiation of Neocortical Progenitor Cells through Independent Mechanisms. J. Neurosci. *22*, 6526–6536. 10.1523/JNEUROSCI.22-15-06526.2002.

103. Tao, W., and Lai, E. (1992). Telencephalon-restricted expression of BF-1, a new member of the HNF-3/fork head gene family, in the developing rat brain. Neuron *8*, 957–966. 10.1016/0896-6273(92)90210-5.
104. Miyoshi, G., and Fishell, G. (2012). Dynamic FoxG1 expression coordinates the integration of multipolar pyramidal neuron precursors into the cortical plate. Neuron *74*, 1045–1058. 10.1016/j.neuron.2012.04.025.
105. Lakso, M., Pichel, J.G., Gorman, J.R., Sauer, B., Okamoto, Y., Lee, E., Alt, F.W., and Westphal, H. (1996). Efficient in vivo manipulation of mouse genomic sequences at the zygote stage. Proc. Natl. Acad. Sci. U. S. A. *93*, 5860–5865. 10.1073/pnas.93.12.5860.
106. Kakizaki, T., Sakagami, H., Sakimura, K., and Yanagawa, Y. (2017). A glycine transporter 2-Cre knock-in mouse line for glycinergic neuron-specific gene manipulation. IBRO Rep. *3*, 9–16. 10.1016/j.ibror.2017.07.002.
107. Feng, G., Mellor, R.H., Bernstein, M., Keller-Peck, C., Nguyen, Q.T., Wallace, M., Nerbonne, J.M., Lichtman, J.W., and Sanes, J.R. (2000). Imaging Neuronal Subsets in Transgenic Mice Expressing Multiple Spectral Variants of GFP. Neuron *28*, 41–51. https://doi.org/10.1016/S0896-6273(00)00084-2.
108. Caberlotto, E., Michel, V., Foucher, I., Bahloul, A., Goodyear, R.J., Pepermans, E., Michalski, N., Perfettini, I., Alegria-Prévot, O., Chardenoux, S., et al. (2011). Usher type 1G protein sans is a critical component of the tip-link complex, a structure controlling actin polymerization in stereocilia. Proc. Natl. Acad. Sci. U. S. A. *108*, 5825–5830. 10.1073/pnas.1017114108.
109. Madisen, L., Zwingman, T.A., Sunkin, S.M., Oh, S.W., Zariwala, H.A., Gu, H., Ng, L.L., Palmiter, R.D., Hawrylycz, M.J., Jones, A.R., et al. (2010). A robust and high-throughput Cre reporting and characterization system for the whole mouse brain. Nat. Neurosci. *13*, 133–140. 10.1038/nn.2467.
110. Sousa, V.H., Miyoshi, G., Hjerling-Leffler, J., Karayannis, T., and Fishell, G. (2009). Characterization of Nkx6-2-derived neocortical interneuron lineages. Cereb. Cortex N. Y. N 1991 *19*, i1–i10. 10.1093/cercor/bhp038.
111. Madisen, L., Mao, T., Koch, H., Zhuo, J.M., Berenyi, A., Fujisawa, S., Hsu, Y.W.A., Garcia, A.J., Gu, X., Zanella, S., et al. (2012). A toolbox of Cre-dependent optogenetic transgenic mice for light-induced activation and silencing. Nat. Neurosci. *15*, 793–802. 10.1038/nn.3078.
112. Connelly, C.J., Ryugo, D.K., and Muniak, M.A. (2017). The effect of progressive hearing loss on the morphology of endbulbs of Held and bushy cells. Hear. Res. *343*, 14–33. 10.1016/j.heares.2016.07.004.
113. Matsumoto, K., Mitani, T.T., Horiguchi, S.A., Kaneshiro, J., Murakami, T.C., Mano, T., Fujishima, H., Konno, A., Watanabe, T.M., Hirai, H., et al. (2019). Advanced CUBIC tissue clearing for whole-organ cell profiling. Nat. Protoc. *14*, 3506–3537. 10.1038/s41596-019-0240-9.
114. Susaki, E.A., Tainaka, K., Perrin, D., Yukinaga, H., Kuno, A., and Ueda, H.R. (2015). Advanced CUBIC protocols for whole-brain and whole-body clearing and imaging. Nat. Protoc. *10*, 1709–1727. 10.1038/nprot.2015.085.
115. Rothman, J.S., and Silver, R.A. (2018). NeuroMatic: An Integrated Open-Source Software Toolkit for Acquisition, Analysis and Simulation of Electrophysiological Data. Front. Neuroinformatics *12*. https://doi.org/10.3389/fninf.2018.00014.
116. Hines, M.L., and Carnevale, N.T. (1997). The NEURON simulation environment. Neural Comput. *9*, 1179–1209. 10.1162/neco.1997.9.6.1179.

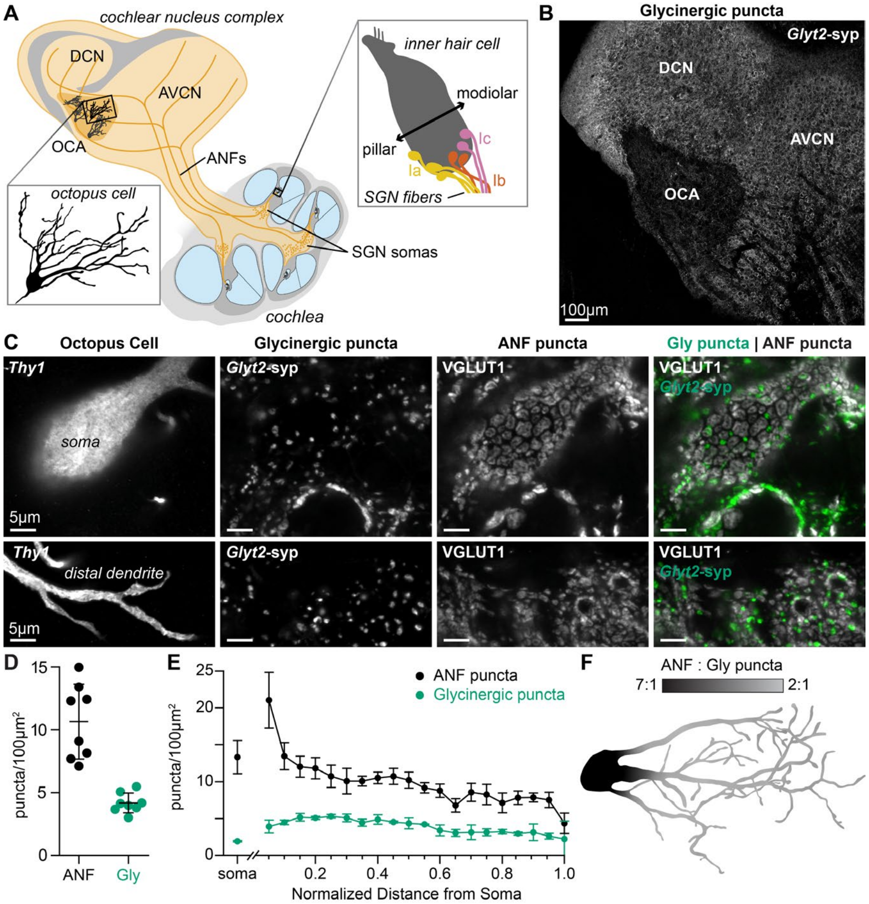

Figure 1. Excitatory and inhibitory synapses to octopus cells form two domains.

(A) Illustration of auditory nerve fiber (ANF) projections into the cochlear nucleus complex (CNC) of the mouse. Octopus cells (left inset) are found in the octopus cell area (OCA) of the ventral cochlear nucleus. Other divisions include the dorsal cochlear nucleus (DCN) and anteroventral cochlear nucleus (AVCN). Three molecular subtypes of spiral ganglion neurons (SGNs) have peripheral fiber projections to hair cells (right inset); subtypes (Ia, Ib, Ic) are organized along the pillar-modiolar axis of inner hair cells.

(B) Glycinergic synaptic puncta (*Glyt2*-syp) in a parasagittal section of the CNC. While the teardrop shaped OCA is not devoid of inhibitory inputs, there are noticeably fewer in the OCA than in the DCN and AVCN.

(C) A Thy1 sparsely labeled octopus cell is closely opposed to inhibitory (*Glyt2*-syp) and ANF (VGlut1) puncta. Micrographs of 3µm confocal z-stacks show puncta on the medial surface of a soma and on a distal dendrite.

(D) Puncta density per 100µm^2 for excitatory ANF (*Foxg1*-syp, black: 10.7 ± 3.0, *n* = 8 cells, 4 mice) and glycinergic puncta (*Glyt2*-syp, green: 4.2 ± 0.8, *n* = 8 cells, 3 mice) on octopus cell dendrites. Data are presented as mean ± SD.

(E) Puncta density per 100µm^2 of soma surface area (ANF, black: 13.3 ± 2.2, *n* = 8 cells, 4 mice; Gly, green: 1.8 ± 0.1, *n* = 8 cells, 3 mice) and density along the length of the dendritic tree, relative to the soma. Data are presented as mean ± SEM.

(F) Illustration of an octopus cell and the ratio between excitatory ANF puncta and glycinergic puncta.

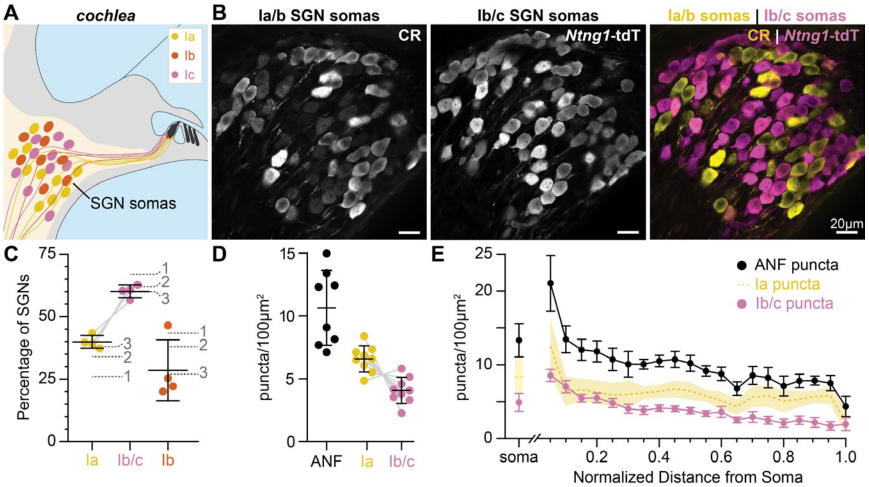

Figure 2. Ia ANFs are the primary excitatory contributors to octopus cells.

(A) Illustration of SGN somas with diverse molecular identities (Ia, yellow; Ib, orange; and Ic, magenta) in a section of the cochlea.

(B) 65µm cochlear section containing SGN somas. SGNs have variable levels of calretinin (CR) immunolabeling corresponding to the three molecular subtypes. Ia/b SGN somas label with high (CR++) and medium (CR+) levels of CR, respectively. Ic somas label with very low levels of CR (CR-). *Ntng1*^{Cre}-mediated expression of tdT (*Ntng1*-tdT) labels Ib/c SGNs.

(C) tdT-CR++ SGNs (Ia) make up 39.9 ± 2.6% of the SGN population. tdT+ SGNs (Ib/c) make up 60.1 ± 2.6% of the SGN population. tdT+CR+ SGNs (Ib) make up 28.5 ± 12.2% of the SGN population. (*n* = 1599 neurons, 4 mice). Data are presented as mean ± SD; individual data points represent percent coverage per animal, lines connect measurements from the same animal. Dotted grey lines are corresponding subtype percentages from 1: Petitpré et al. 2018, 2: Shrestha et al. 2018, and 3: Sun et al. 2018.

(D) Puncta density per 100µm^2 for all ANFs (black: data from Fig 1D), Ia ANFs (yellow: 6.6 ± 1.0), and Ib/c ANFs (magenta: 4.1 ± 1.0, *n* = 9 cells, 5 mice) on octopus cell dendrites. Ia density was calculated by subtracting Ib/c density from total ANF density; lines connect measurements from the same reconstruction. Data are presented as mean ± SD.

(E) Puncta density per 100µm^2 of soma surface area (all ANF, black: data from Fig 1E; Ia ANFs, yellow: 8.4 ± 2.3; and Ib/c ANFs, magenta: 4.9 ± 1.2, *n* = 9 cells, 5 mice) and density along the length of the dendritic tree, relative to the soma. Data are presented as mean ± SEM.

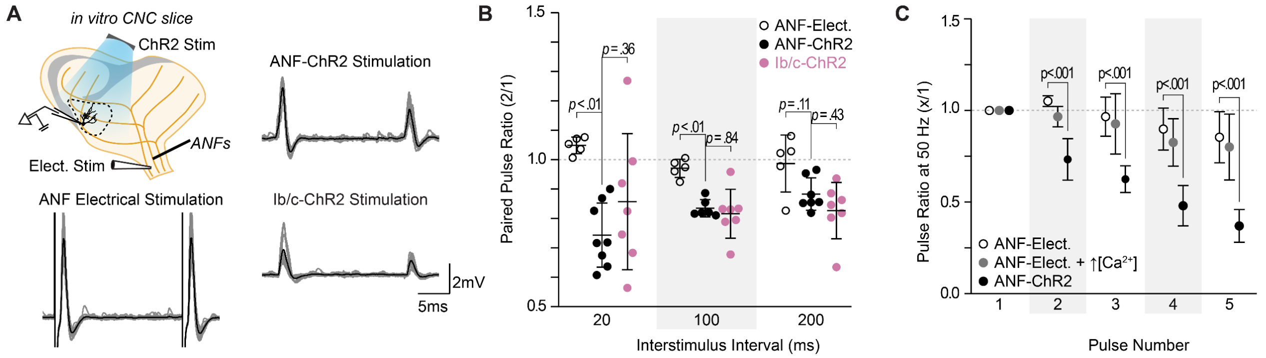

Figure 3. ANF subpopulation synapses with octopus cells do not differ in short term dynamics.

(A) Illustration of experimental paradigm and representative EPSPs recorded from *in vitro* whole-cell current clamp recordings of octopus cells. ANF stimulation method included electrical stimulation or full-field light-evoked ChR2 activation.

(B) Paired pulse ratios for electrically stimulated ANFs (open circles: *n* = 5 cells, 3 mice), ChR2 stimulated ANFs (black: *n* = 8 cells, 5 mice), and ChR2 stimulated Ib/c ANFs (magenta: *n* = 7 cells, 6 mice) at three interstimulus intervals. With electrical stimulation, ANF inputs to octopus cells were stable and exhibited slight facilitation at 50 Hz (20ms interstimulus interval). Full-field and axon-targeted ChR2 stimulation caused paired pulse depression not seen in electrical simulation. Data are presented as mean ± SD. Markers represent the average paired pulse ratio for a cell. *p* values from ANOVA and subsequent Tukey HSD test are reported for comparisons between methods of ANF activation (electrical and ChR2) and ANF subpopulation composition within method of activation (ANF-ChR2 and Ib/c-ChR2). Welch's ANOVA was used for comparisons at 20ms interstimulus interval (50Hz) as data in this condition did not meet the homogeneity of variance assumption.

(C) Pulse ratios at 50Hz for electrically stimulated ANFs (open circles: *n* = 5 cells, 3 mice), electrically stimulated ANFs in ACSF with 2.4mM $CaCl_2$ and 1.3mM $MgSO_4$ (grey: *n* = 3 cells, 2 mice) and ChR2 stimulated ANFs (black: *n* = 8 cells, 5 mice). Data are presented as mean ± SD. $p < 0.001$ from ANOVA and subsequent Tukey HSD test for all comparisons between methods of ANF activation (electrical and ChR2). There were no statistically significant differences for all comparisons under 1.4mM $CaCl_2$ and 2.4mM $CaCl_2$ ($p > 0.100$, ANOVA).

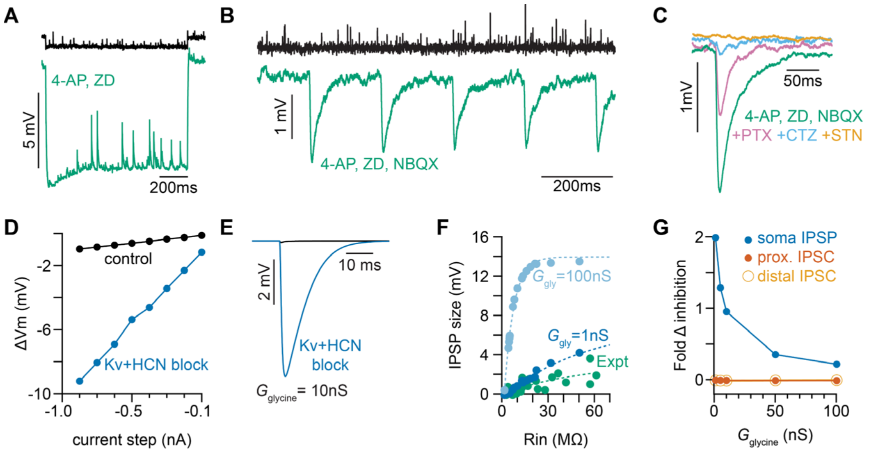

Figure 4. Octopus cells receive glycinergic inhibitory post synaptic potentials.

(A) Voltage responses to a -200pA hyperpolarizing current injection in an *in vitro* whole-cell current clamp recording of an octopus cell. This representative neuron hyperpolarized 0.7 mV (black). After bath application of 100µM 4-Aminopyridine (4-AP) and 50µM ZD 7288 (ZD), hyperpolarizing responses to the same -200pA current injection increased to 8.8 mV at steady state (green).

(B) Representative postsynaptic responses to ChR2 stimulation of glycinergic terminals with a 5Hz train of 1ms full-field blue light pulses before (black) and after bath application of 100µM 4-AP, 50µM ZD, and 15µM NBQX (green: *n* = 9 cells, 8 mice). Increased input resistance reveals inhibitory potentials that are difficult to detect during somatic recordings.

(C) Representative postsynaptic responses to ChR2 stimulation of glycinergic terminals after bath application of 100µM 4-AP, 50µM ZD, and 15µM NBQX (green), then the further addition of 20µM picrotoxin (PTX) to block homomeric glycine receptors (pink), 100µM cyclothiazide (CTZ), to block α2-containing glycine receptors (blue), and 500nM strychnine (STN) to block any remaining heteromeric glycine receptors (orange; *n* = 6 cells, 5 mice).

(D) Change in membrane voltage in response to a series of hyperpolarizing somatic current steps in a morphologically and biophysically realistic model of octopus cells before (black) and after removal of voltage-gated potassium (K_v) and hyperpolarization-activated cyclic nucleotide-gated (HCN) channels (blue). Comparable to current-clamp recordings in A, removing K_v and HCN channels in the model increased the magnitude of voltage responses (ΔVm) to hyperpolarizing current steps.

(E) IPSPs recorded at the soma of a modeled octopus cell before (black) and after removal of K_v and HCN channels (blue). Comparable to the recordings in *(B)*, blocking these channels allows for IPSP detection at the soma.

(F) IPSP magnitude in experimental data (green) and the model (blue) as a function of input resistance. In somatic recordings, detectable IPSP size increases with input resistance. Modeled IPSPs are shown for two conductance levels (1nS, dark blue; 100nS light blue).

(G) Fold change in magnitude of soma-measured IPSPs (blue) or dendrite-measured IPSCs at proximal (dark orange) and distal (light orange) dendritic locations after removal of K_v and HCN channels in the model. While input resistance changes impact the magnitude of soma-measured IPSPs, the size of dendritic currents are not changed.

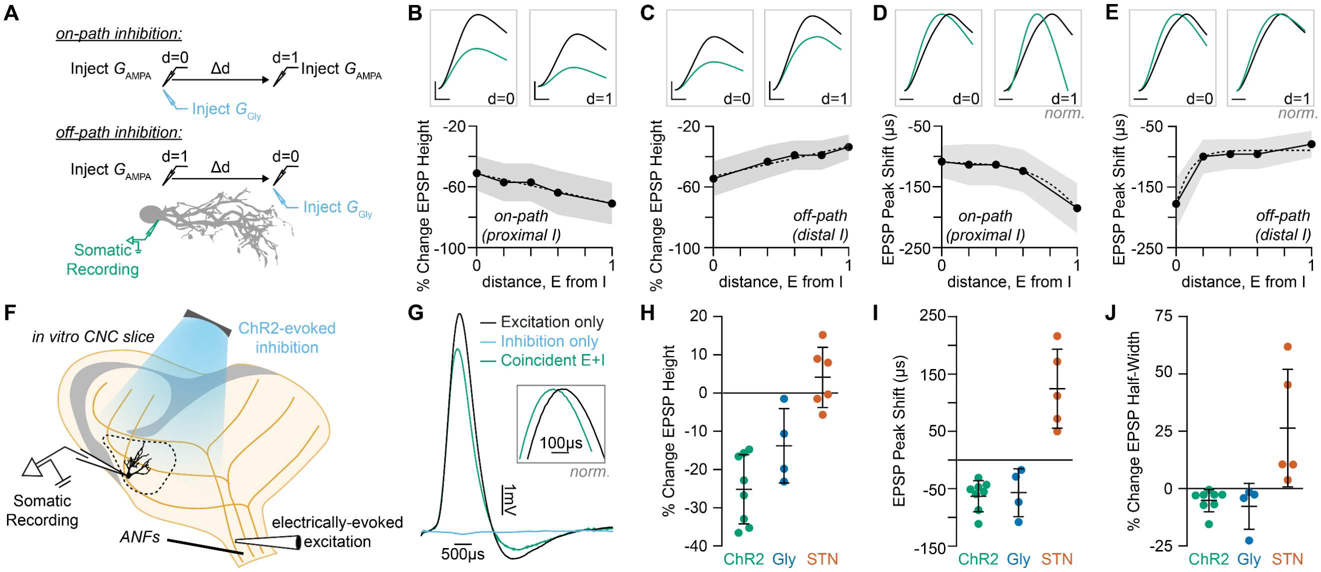

Figure 5. Coincident excitation and inhibition on octopus cell dendrites advances EPSP peak times.

(A) The impact of distance between excitatory and inhibitory synapses in a morphologically and biophysically realistic model of octopus cells. Inhibitory synapses were placed either proximally (on-path inhibition) or distally (off-path inhibition) to excitation. Excitatory synapses were placed at varying locations along the dendritic arbor to change the anatomical distance (Δd) between excitation and inhibition. EPSPs were measured at the soma.

(B-C) Quantification of the percent change in soma-measured EPSP magnitude in models of on-path inhibition *(B)* and off-path inhibition *(C)*. Example traces show EPSPs with (green) and without (black) inhibition at d=0 and d=1. Inset scale bars are 1mV, 200ms.

(D-E) Quantification of the shift in EPSP peak timing in models of on-path inhibition *(D)* and off-path inhibition *(E)*. Example traces show normalized EPSPs with (green) and without (black) inhibition at d=0 and d=1. Inset scale bar is 200ms.

(F) Illustration of *in vitro* experimental paradigm in which ANFs are stimulated electrically and glycinergic terminals are activated with a 1ms pulse of full-field blue light during whole-cell current clamp recordings.

(G) Representative responses to independent stimulation of excitatory ANFs (black), inhibitory inputs (blue), and coincident stimulation of both excitation and inhibition (green). Inset shows normalized peaks for excitation alone (black) and coincident excitation and inhibition (green).

(H-J) Quantification the percent change in EPSP magnitude *(H)*, the shift in EPSP peak timing *(I)*, and the percent change in EPSP half-width *(J)* during coincident ChR2 activation of inhibitory inputs (green: *n* = 8 cells, 6 mice), bath application of 25µM glycine (blue: *n* = 4 cells, 3 mice), and bath application of 1µM STN (orange: *n* = 5 cells, 4 mice). Activation of glycinergic receptors during excitation decreases EPSP heights and advances EPSP peaks with little change to EPSP half-width. Blocking of tonically active glycine receptors has the opposite effect. Data are presented as mean ± SD. Markers represent the average quantification for a cell.

Supplemental Table 1: Summary and description of experimental genotypes used in experiments.

	Experimental Genotype	*Abbreviation*	*Description*
Fig. 1B	*Glyt2*$^{Cre/+}$; Ai34$^{tg/+}$	*Glyt2*-syp	syp-tdT in *Glyt2* inhibitory neurons
Fig. 1C	*Glyt2*$^{Cre/+}$; Ai34$^{tg/+}$; Thy1$^{tg/+}$	*Glyt2*-syp; Thy1	syp-tdT in *Glyt2* inhibitory neurons; YFP octopus cells
Fig. 1D-E, black	*Foxg1*$^{Cre/+}$; Ai34$^{tg/+}$; Thy1$^{tg/+}$	*Foxg1*-syp; Thy1	syp-tdT in *Foxg1* ANFs; YFP octopus cells
Fig. 1D-E, green	*Glyt2*$^{Cre/+}$; Ai34$^{tg/+}$; Thy1$^{tg/+}$	*Glyt2*-syp; Thy1	syp-tdT in *Glyt2* inhibitory neurons; YFP octopus cells
Fig. 2B-C	*Ntng1*$^{Cre/+}$; Ai14$^{tg/+}$; *Foxg1*$^{Flp/+}$; RCE:FRT$^{tg/+}$	*Ntng1*-tdT; *Foxg1*-EYFP	tdT in *Ntng1* Ib/c ANFs; EYFP in all ANFs
Fig. 2D-E	*Ntng1*$^{Cre/+}$; Ai34$^{tg/+}$; Thy1$^{tg/+}$	*Ntng1*-syp; Thy1	syp-tdT in *Ntng1* Ib/c ANFs; YFP octopus cells
SFig. 1C-E	*Ntng1*$^{Cre/+}$; Ai14$^{tg/+}$; *Foxg1*$^{Flp/+}$; RCE:FRT$^{tg/+}$	*Ntng1*-tdT; *Foxg1*-EYFP	tdT in *Ntng1* Ib/c ANFs; EYFP in all ANFs
SFig. 1F	*Ntng1*$^{Cre/+}$; Ai14$^{tg/+}$	*Ntng1*-tdT	tdT in *Ntng1* Ib/c ANFs and other neurons
SFig. 1G	*Ntng1*$^{Cre/+}$; Ai34$^{tg/+}$	*Ntng1*-syp	syp-tdT in *Ntng1* Ib/c ANFs
SFig. 2A-F	*Myo15*$^{iCre/+}$; Ai14$^{tg/+}$; *Foxg1*$^{Flp/+}$; RCE:FRT$^{tg/+}$	*Myo15*-tdT; *Foxg1*-EYFP	tdT in *Myo15* Ic ANFs; EYFP in all ANFs
SFig. 2G-I	*Myo15*$^{iCre/+}$; Ai34$^{tg/+}$; Thy1$^{tg/+}$	*Myo15*-syp; Thy1	syp-tdT in *Myo15* Ic ANFs; YFP octopus cells
Fig. 3A-C, black	*Foxg1*$^{Cre/+}$; Ai32$^{tg/+}$	*Foxg1*-ChR2	ChR2 in *Foxg1* ANFs
Fig. 3A-C, magenta	*Ntng1*$^{Cre/+}$; Ai32$^{tg/+}$	*Ntng1*-ChR2	ChR2 in *Ntng1* Ib/c ANFs
Fig. 4A-C	*Glyt2*$^{Cre/+}$; Ai32$^{tg/+}$	*Glyt2*-ChR2	ChR2 in *Glyt2* inhibitory neurons
Fig. 5F-J	*Glyt2*$^{Cre/+}$; Ai32$^{tg/+}$	*Glyt2*-ChR2	ChR2 in *Glyt2* inhibitory neurons

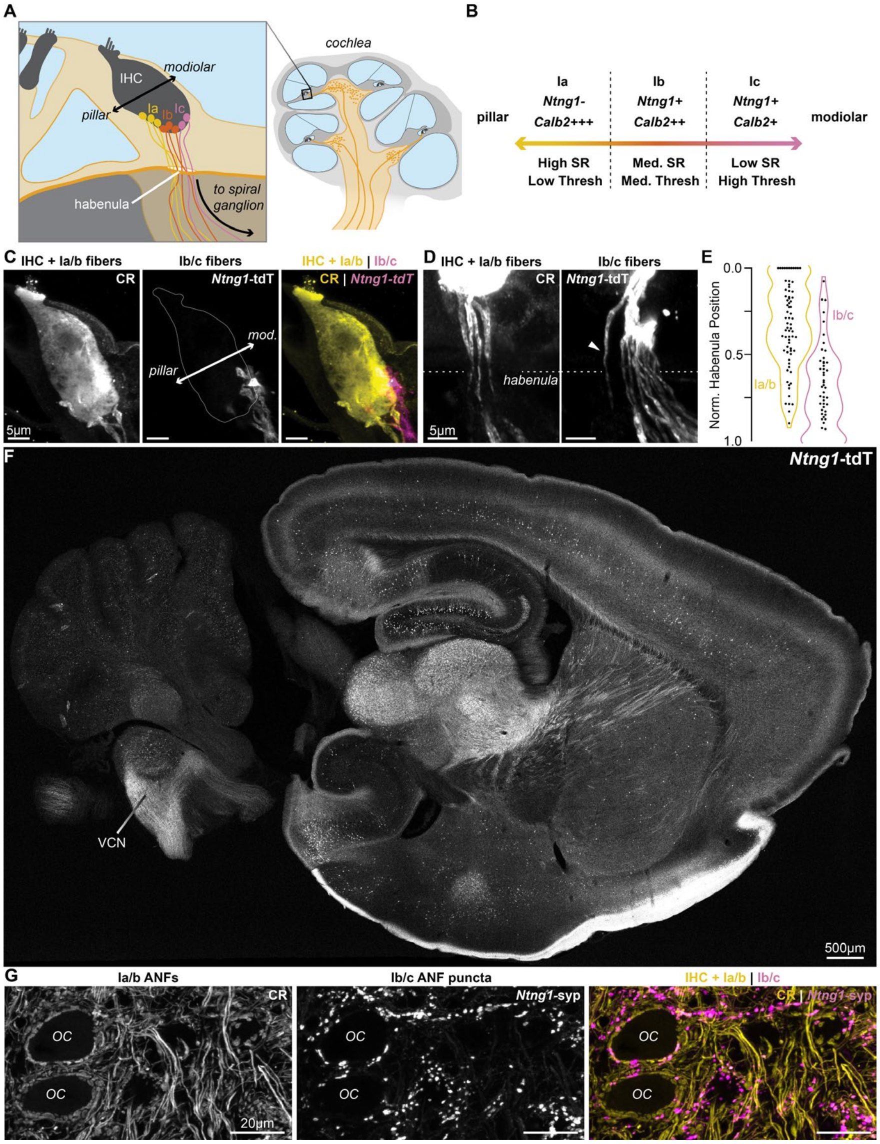

Supplemental Figure 1.
***Ntng1*^{Cre} has high specificity for Ib/c SGNs.**

(A) Illustration of SGNs and their peripheral synapses with inner hair cells (IHCs). Peripheral synapses of SGN subtypes are organized along the pillar-modiolar axis of IHCs and through the habenula. Ib/c SGN peripheral fibers are positioned on the modiolar side of the IHC, i.e. closest to the spiral ganglion, whereas Ia fibers are on the other side, i.e. closest to the pillar cells in the organ of Corti.

(B) Anatomical and molecular properties of SGNs are correlated. Strongly calretinin immunopositive and *Calb2* expressing Ia fibers innervate the pillar side of IHCs. *Ntng1* expressing Ib/c fibers innervate the modiolar side of IHCs. These properties correlate with spontaneous rates (SR) and thresholds measured *in vivo*.

(C) Calretinin immunopositive (CR+) Ia/b fibers (CR, yellow) preferentially innervate the pillar side of IHCs. Ib/c fibers with *Ntng1*^{Cre}-mediated expression of tdTomato (*Ntng1*-tdT, magenta) preferentially innervate the modiolar side of IHCs. IHCs also immunolabel for CR.

(D) CR+ Ia/b fibers (yellow) pass through the pillar side of the habenula while *Ntng1*-tdT+ Ib/c fibers (magenta) pass through the modiolar side. Arrowhead highlights a *Ntng1*-tdT fiber passing through the pillar side of the habenula but ultimately terminating on the modiolar side of the hair cell.

(E) Normalized position of CR+ Ia/b (yellow) and *Ntng1*-tdT+ Ib/c (magenta) fibers along the pillar to modiolar axis of the habenula (*n* = 124 fibers; 5 mice).

(F) In the central nervous system, *Ntng1*-tdT is present throughout the whole brain, but is restricted to ANFs in the ventral cochlear nucleus (VCN) where the octopus cell area (OCA) is found.

(G) In the OCA, CR immunolabel is present in Ia/b ANFs and puncta. As in the ganglion (Figure 2B), CR co-labels with some Ib/c puncta (*Ntng1*-syp).

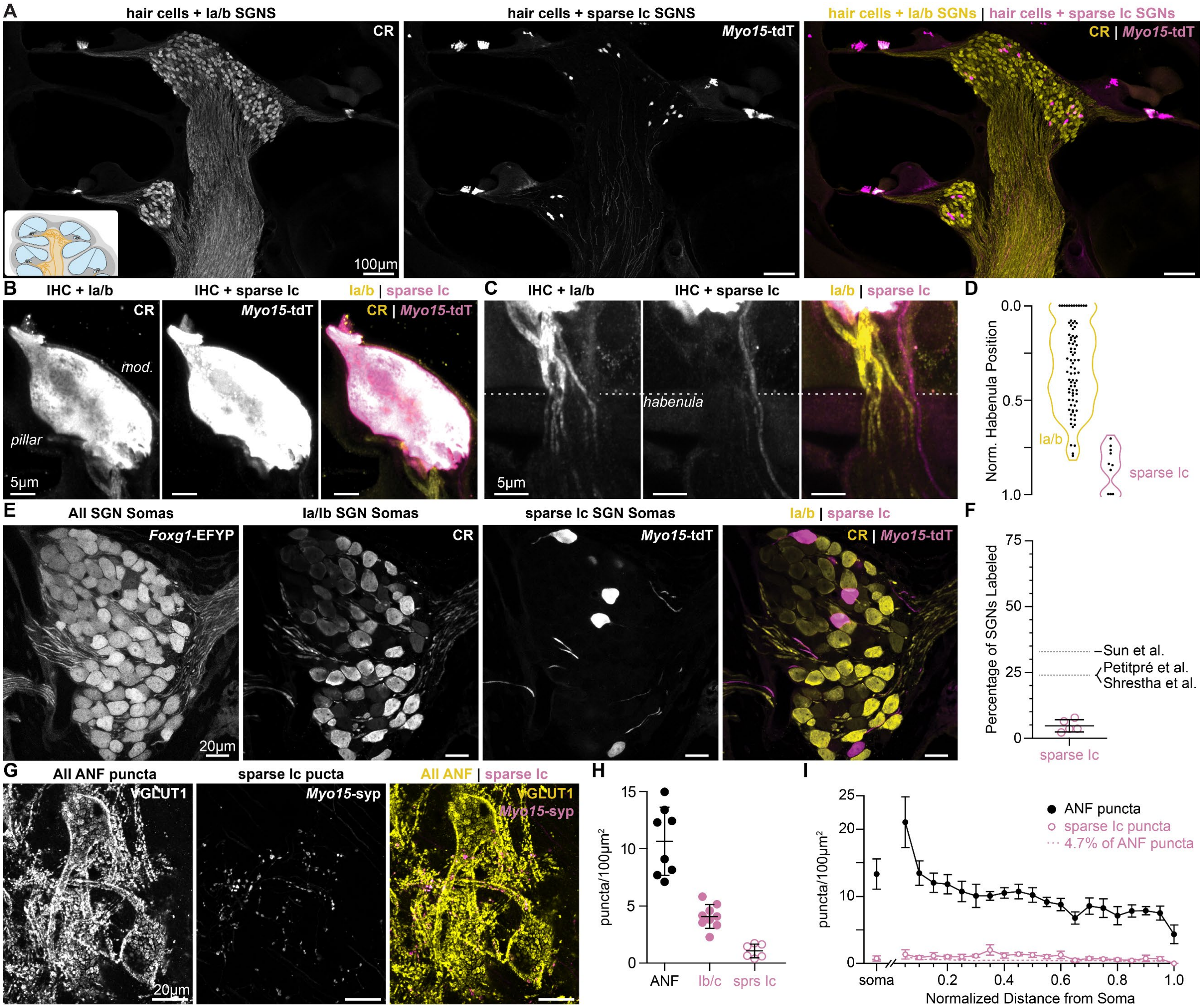

Supplemental Figure 2. *Myo15*^{iCre} sparsely labels Ic SGNs.

(A) Cochlear sections with calretinin (CR) immunolabeling of hair cells and type Ia/b SGNs and *Myo15*^{iCre}-mediated expression of tdTomato (*Myo15*-tdT) in hair cells and some type Ic SGNs.

(B) CR+ Ia/b fibers (yellow) preferentially innervate the pillar side of IHCs. Sparse Ic fibers with *Myo15*^{iCre}-mediated expression of tdTomato (*Myo15*-tdT, magenta) preferentially innervate the modiolar side of IHCs. IHCs label with both tdT and CR.

(C) CR+ Ia/b fibers (yellow) pass through the pillar side of the habenula while sparsely labeled *Myo15*-tdT+ Ic fibers (magenta) pass through the modiolar side.

(D) Normalized position of CR+ Ia/b (yellow) and *Myo15*-tdT+ Ic (magenta) fibers along the pillar to modiolar axis of the habenula (*n* = 90 fibers; 4 mice).

(E) 65µm cochlear section containing SGN somas. SGNs have variable levels of calretinin (CR) immunolabeling corresponding to the three molecular subtypes. Ia/b SGN somas label with high and medium levels of CR, respectively. Ic somas label with very low levels of CR. *Myo15*-tdT is sparsely found in Ic SGNs. All SGN somas are labeled with *Foxg1*^{Cre}-mediated expression of EYFP (*Foxg1*-EYFP).

(F) tdT+CR- SGNs make up 4.7 ± 2.3% of the SGN population (*n* = 2150 neurons, 5 mice), indicating sparse reporter expression. Data are presented as mean ± SD; individual data points signify percent coverage per animal. Dotted lines are estimated percentages for type Ic SGNs from 1: Petitpré et al., 2018, 2: Shrestha et al., 2018, and 3: Sun et al., 2018.

(G) In the OCA, VGlut1 immunolabel neatly tiles around octopus cells with sparse *Myo15*-syp puncta.

(H) Density of all ANFs (black: data from Fig 1D), Ib/c ANFs (magenta: data from Fig 2D), and sparse Ic inputs (open magenta circles: 1.1 ± 0.6, *n* = 6 cells, 3 mice). Data are presented as mean ± SD. Markers represent the total puncta density computed per reconstructed octopus cell.

(I) Puncta density per 100µm^2 of soma surface area (all ANF, black: data from Fig 1E; sparse I/c inputs, magenta open circles: 0.7 ± 0.4, *n* = 6 cells, 3 mice) and density along the length of the dendritic tree, relative to the soma. Data are presented as mean ± SEM.

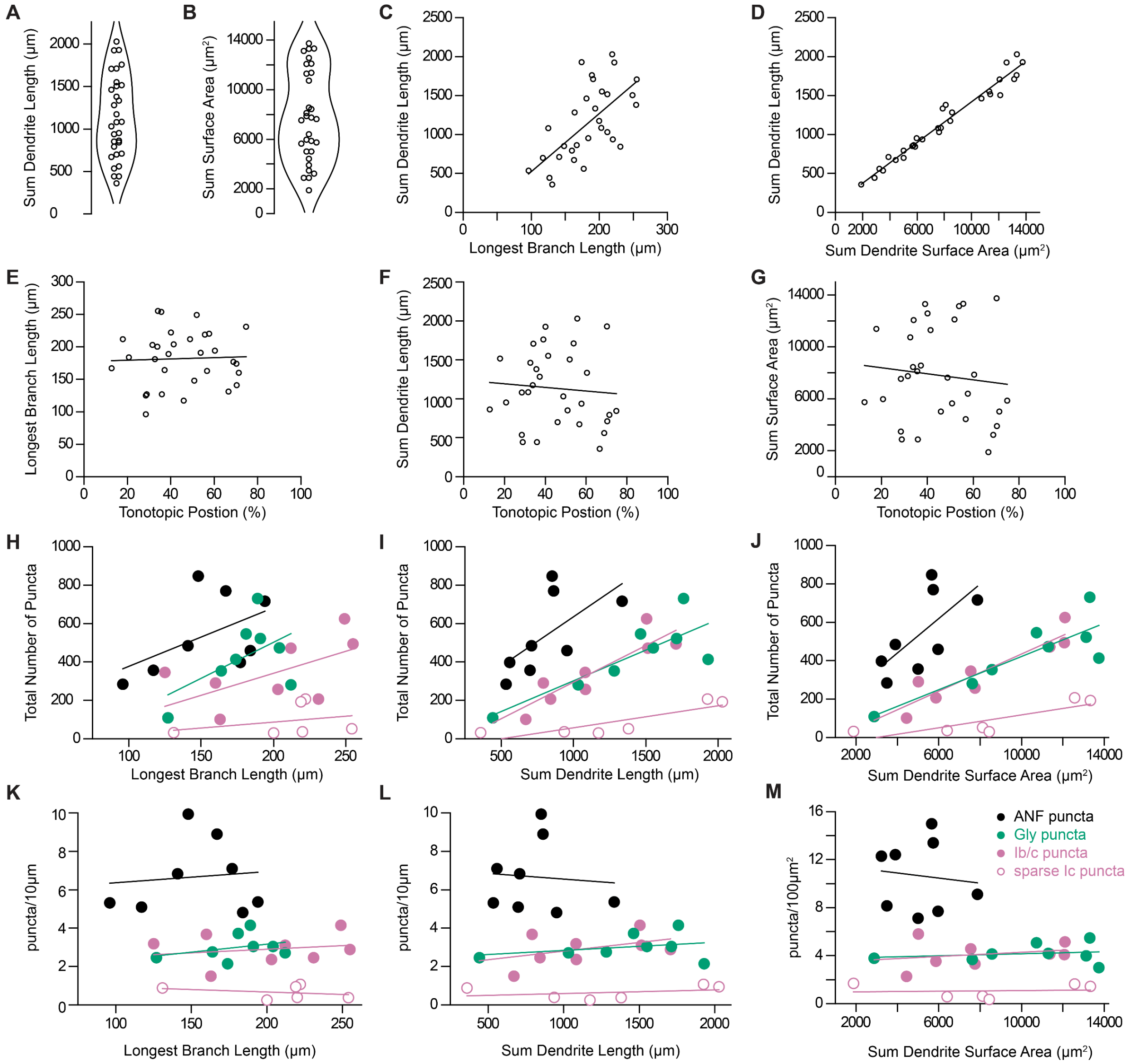

Supplemental Figure 3. Dendritic and synaptic reconstructions of octopus cells.

(A) Total length of reconstructed dendritic arbors for 31 octopus cells.

(B) Total surface area of reconstructed dendritic arbors for 31 octopus cells.

(C) Octopus cell reconstructions were normalized to the longest reconstructed dendrite. Total length of reconstructed dendrites correlated with the longest branch per neuron.

(D) Total length of reconstructed dendrites correlated with total dendritic surface area.

(E-G) Longest branch length, total dendrite length, and total surface area compared to estimated position of the octopus cell soma in the tonotopic organization of the OCA.

(H-J) Total number of reconstructed ANF puncta (*Foxg1*-syp, black), inhibitory puncta (*Glyt2*-syp, green), Ib/c ANF puncta (*Ntng1*-syp, magenta), and sparse Ic ANF puncta (*Myo15*-syp, open magenta circles) compared to the longest branch length, total dendrite length, and total dendrite surface area.

(K-M) Density of reconstructed ANF puncta (*Foxg1*-syp, black), inhibitory puncta (*Glyt2*-syp, green), Ib/c ANF puncta (*Ntng1*-syp, magenta), and sparse Ic ANF puncta (*Myo15*-syp, open magenta circles) compared to longest branch length, total dendrite length, and total dendrite surface area.

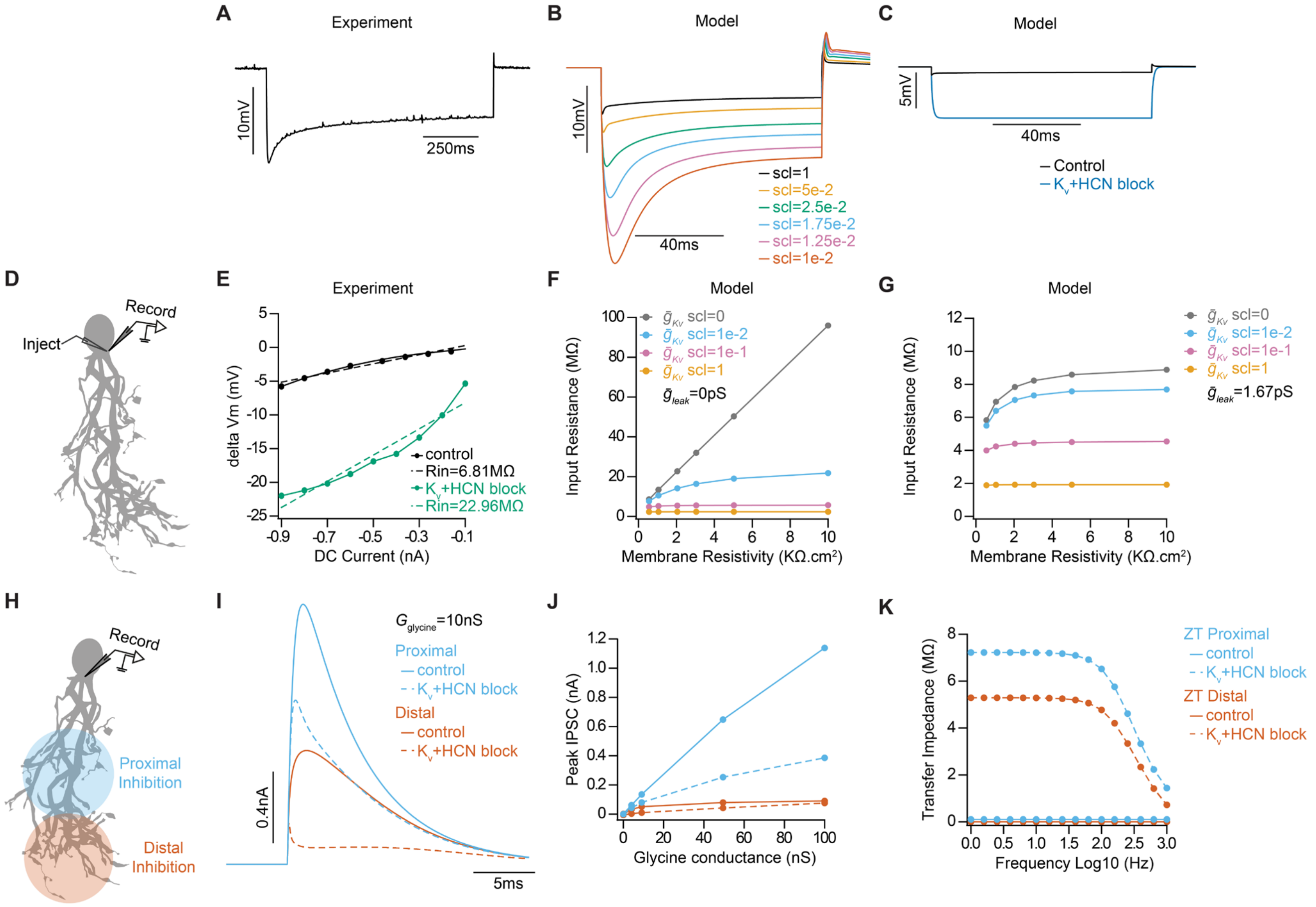

Supplemental Figure 4. Optimizing active and passive properties of an octopus cell model.

(A) Subthreshold somatic voltage response to a hyperpolarizing current injection in an *in vitro* whole-cell current clamp recording of an octopus cell.

(B) Somatic voltage responses from a morphologically realistic octopus cell model for various scaling factors of maximal conductances of active ion-channels.

(C) Comparison of somatic hyperpolarizations in a model reproducing experimental data during control (black) and K_v and HCN block conditions (blue).

(D) Illustration of injection and recording locations for panels *E-G* in a morphologically realistic octopus cell model.

(E) IV curves (change in somatic membrane potential as function of current injection magnitude) from a representative experimental octopus cell. Dotted lines plot linear fits of the experimental data. Rin dotted line is the slope of the fit.

(F-G) Impact of leak conductance ($\bar{g}_{leak}$) and scaling factor (scl) on passive properties of the model. Input resistance of the octopus neuron model as a function of membrane resistivity (Rm) with $\bar{g}_{leak}$=0 *(F)* and $\bar{g}_{leak}$=1.67 pS *(G)* for various scaling factor values indicated in different colors.

(H) Illustration of injection and recording locations for panels *I-K* in a morphologically realistic octopus cell model.

(I) Inhibitory post synaptic currents (IPSCs) recorded from glycinergic synapses in proximal (blue) and distal (orange) stimulation during control (solid) and K_v and HCN block conditions (dotted).

(J) Peak IPSC magnitude as function of glycine conductance in proximal (blue) and distal (orange) stimulation during control (solid) and K_v and HCN block conditions (dotted).

(K) Transfer impedance as function of frequency from proximal dendrites to soma (blue) and distal dendrites to soma (orange) during control (solid) and K_v and HCN block conditions (dotted).

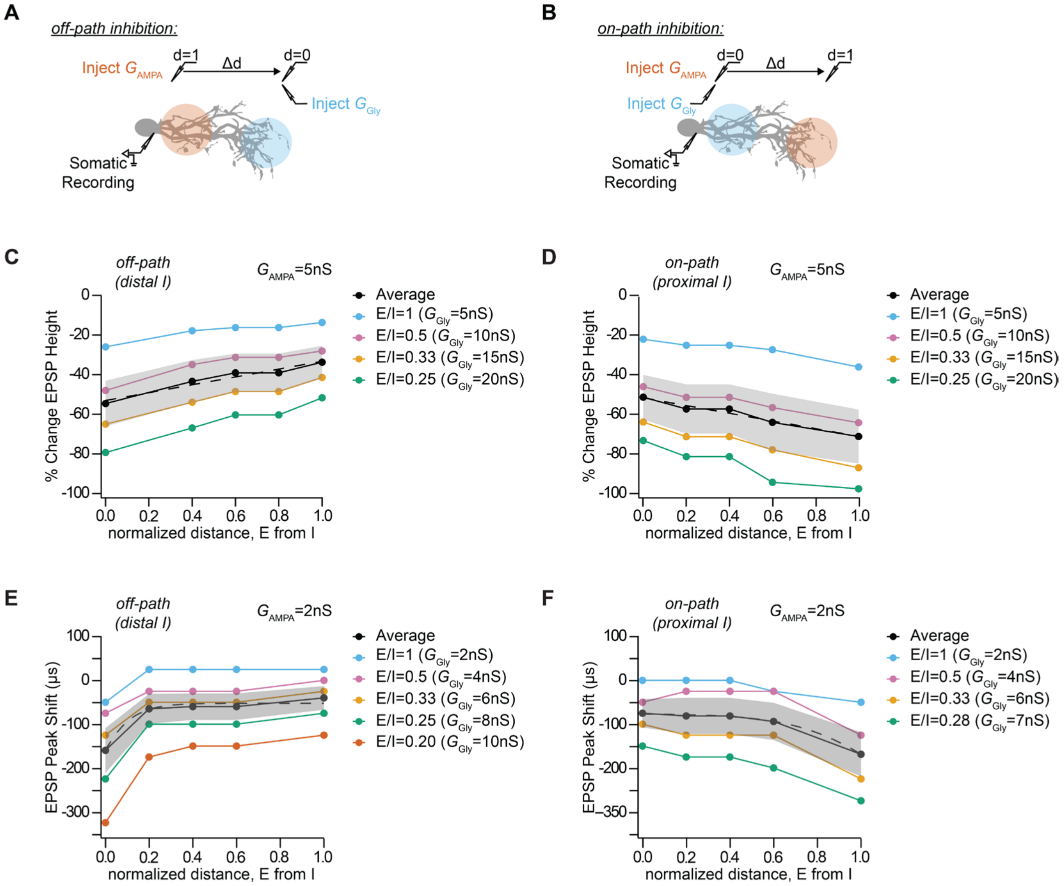

Supplemental Figure 5: Impact of inhibitory synaptic location and distance between excitatory and inhibitory synapse on somatic EPSP amplitude and timing.

(A-B) Illustration of injection and recording locations for off-path *(A)* and on-path *(B)* inhibition paradigms and the normalized relative distance (Δd) between excitatory synapses. The impact of on-path and off-path inhibition in the dendrites is primarily determined by the local potential change by EPSP and the attenuation or the length constant (λ) of the IPSP towards the excitatory synaptic location. The exponential decay of membrane voltage is asymmetric, with lower λ for the open end and higher λ for sealed end propagation. Distal parts of the dendrites have higher local input resistance and lower attenuation of IPSP due to the sealed end.

(C-D) Percentage change in somatic EPSP height with dendritic glycinergic inhibition as function of normalized distance between excitatory and inhibitory synapses in off-path *(C)* and on-path *(D)* inhibition for various E/I ratio with excitatory AMPA conductance (G_{AMPA}) set at 5nS. Average shown in black with SEM in shaded region.

(E-F) Somatic EPSP peak time shift with dendritic glycinergic inhibition as function of normalized distance between excitatory and inhibitory synapses in off-path *(E)* and on-path *(F)* inhibition for various E/I ratio with excitatory AMPA conductance (G_{AMPA}) set at 2nS. Average shown in black with SEM in shaded region.